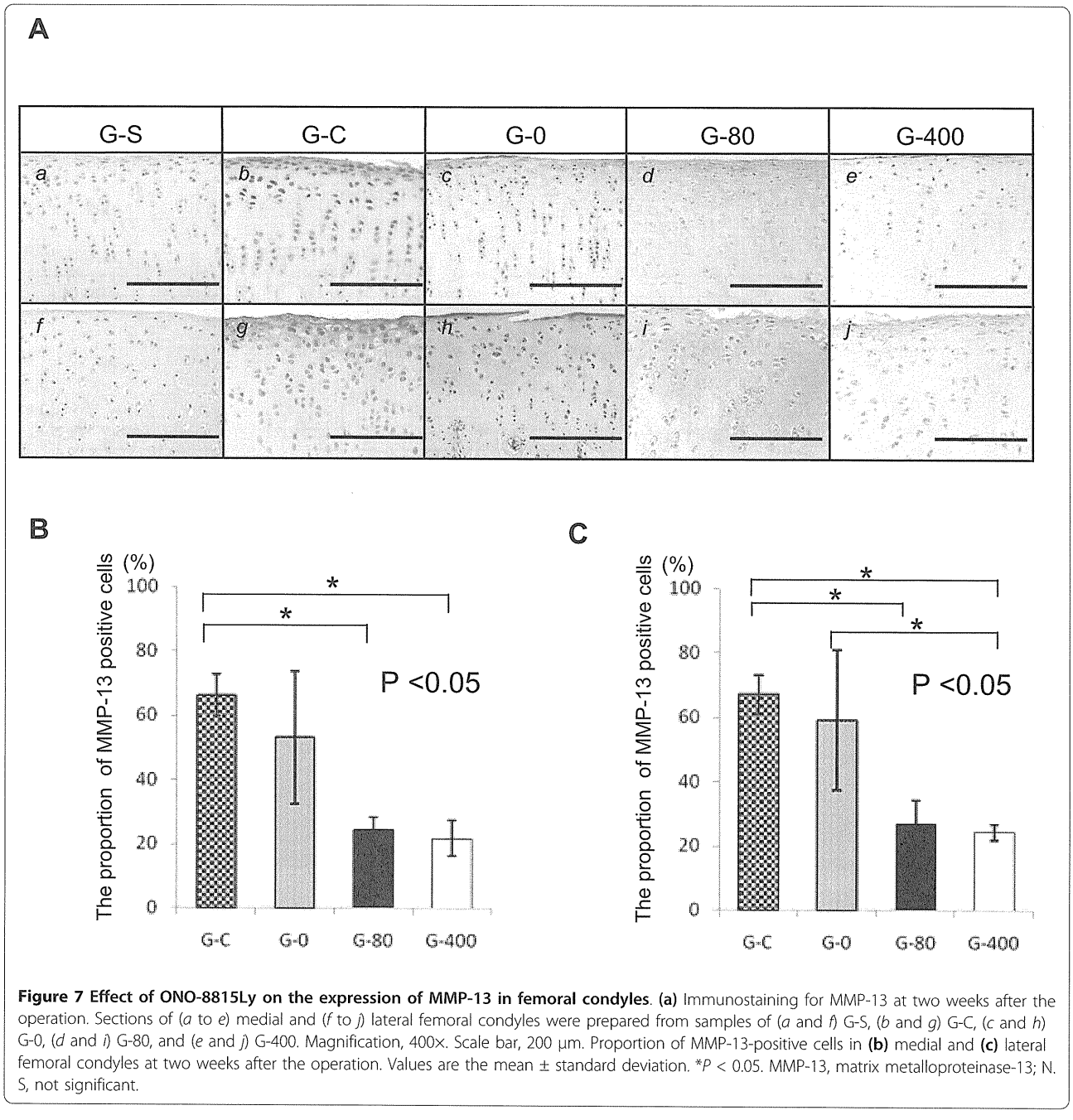

Figure 7 Effect of ONO-8815Ly on the expression of MMP-13 in femoral condyles. **(a)** Immunostaining for MMP-13 at two weeks after the operation. Sections of (*a* to *e*) medial and (*f* to *j*) lateral femoral condyles were prepared from samples of (*a* and *f*) G-S, (*b* and *g*) G-C, (*c* and *h*) G-0, (*d* and *i*) G-80, and (*e* and *j*) G-400. Magnification, 400×. Scale bar, 200 μm. Proportion of MMP-13-positive cells in **(b)** medial and **(c)** lateral femoral condyles at two weeks after the operation. Values are the mean ± standard deviation. *$P < 0.05$. MMP-13, matrix metalloproteinase-13; N. S, not significant.

result. A study has shown that the lateral components of the rabbit knees were more susceptible to degeneration than the medial components in the ACLMT model [31]. The rabbit knee joints are physiologically in the valgus position, causing excess load on the lateral side, which might explain the susceptibility.

The grade of degeneration at 12 weeks was less prominent than we expected (Figure 4). In this injury model, cartilage degeneration will be induced by abnormal stress due to joint instability. Such abnormal stress takes place during weight-bearing movements of the knee joints. Therefore, to enhance such stress, Park et al. forced the rabbits to move in a confined space (5 m × 5 m) for one hour twice a day, from three days after ACLMT onward [22], which increased the Mankin's score up to 12 points at eight weeks after the operation. Restriction in a small cage in the knee-flexed position, as in our study, may minimize such stresses. In addition, both knees were operated on, which may further decrease the activities of the rabbits. These may cause almost no progression of the disease after two weeks.

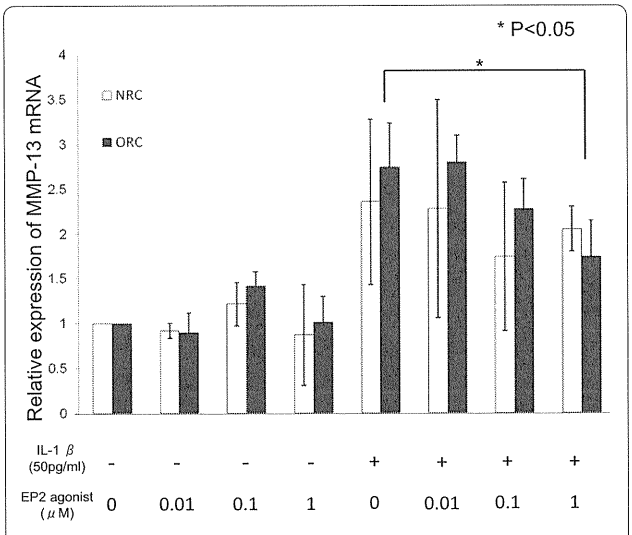

Figure 8 Reduction of IL-1β-induced *MMP-13* mRNA expression by an EP2 agonist on rabbit normal or OA chondrocyte primary culture cells *in vitro*. Expression levels of *MMP-13* mRNA in NRC and ORC at six hours after treatment with IL-1β (50 pg/ml), ONO-AE-259-01, selective EP2 agonist (each at a concentration of 0, 0.01, 0.1, and 1 μM), or a combination of IL-1β and ONO-AE-259-01. GAPDH was used as internal control. Using the ratio obtained for the untreated sample as a standard (1.0), the relative ratio of the treated samples was presented as the relative expression levels of the *MMP-13* gene. Values are the mean ± standard deviation. NRC (n = 4) and ORC (n = 5). *$P < 0.05$. EP2, prostaglandin E2 receptor type 2; IL-1β, interleukin-1β; MMP-13, matrix metalloproteinase-13; NRC, non-treated rabbit chondroctes; ORC, ACLMT-operated rabbit chondrocytes.

Generally, cartilage degeneration in OA is due to the induction of MMP expression. MMP-13 is a product of chondrocytes that reside in cartilage and has a stronger effect that MMP-1 on type II collagen [32]. Some insisted that PGE2 exerts direct inhibitory effects on the expression of MMP-1 [33,34] and MMP-13 [28,33,34] in arthritic chondrocytes, and Sato et al. demonstrated that EP2 signaling was responsible for the down-regulation of MMP-13 *in vitro*, although they used a different agonist [28]. Taken together, EP2 signaling regulates MMP-13 production. In agreement, we showed that production of MMP-13 in articular chondrocytes was reduced when treated with an EP2 agonist *in vivo* (Figure 7) and *in vitro* (Figure 8). Controversially others studies show that PGE2 plays a crucial role in the induction of MMP-13 and MMP-3 in chondrocytes in response to IL-1β in microsomal prostaglandin E synthase-deficient mice [35] or that of PGE2 inhibits chondrocyte maturation [36]. In the current study model, EP2 signaling was shown to inhibit the expression of *MMP-13* mRNA, suggesting that EP2 signaling protects the articular cartilage from degeneration.

MMP-3 is a protease expressed in OA specimens at an early stage [37,38]. MMP-3 cleaves a variety of ECM components such as proteoglycans, collagens, and procollagens [39]. In the current study, ONO-8815Ly had no effect on the production of MMP-3 (Figure 6). Although there is still much to be done, the current study suggested that an EP2 agonist may exert a protective effect on articular cartilage by inhibiting MMP-13.

It is important to clarify whether an EP2 agonist caused inflammation either systemically or locally. PGs are pro-inflammatory lipid mediators whose levels increase in the synovial membrane and synovial fluid of patients with OA. We previously reported that intra-articular administration of an EP2 agonist did not affect the mRNA expression of the *MMP-3*, *TIMP-3*, and *IL-1β* genes in the synovium, or the amounts of TNF-α and C-reactive protein (CRP) in joint fluids. As in our previous study, we found no severe inflammatory changes in the synovium, and no change in the levels of CRP (data not shown), suggesting that this EP2 agonist caused no inflammation either systemically or locally.

The effect of an EP2 agonist did not last long (Figure 4), yet this may be rectified by developing a suitable drug-delivery system. Continuous administration of an EP2 agonist using such a newly developed system could provide a novel therapeutic modality to treat OA.

Conclusions

Stimulation of PGE2 via EP2 prevents degeneration of the articular cartilage during the early stages. The current study suggests that EP2 agonists may exert a protective effect on articular cartilage by inhibiting MMP-13. With a long-term delivery system, the EP2 agonist could be a new therapeutic tool for OA.

Abbreviations

ACLMT: anterior cruciate ligament and menisectomy transaction; COX: cyclo-oxygenase; CRP: C-reactive protein; DMEM: Dulbecco's modified Eagle's medium; ECM: extracellular matrix; EP2: prostaglandin E2 receptor type 2; FBS: fetal bovine serum; GAPDH: glyceraldehyde 3-phosphate dehydrogenase; H&E: hematoxylin & eosin; IGF: insulin-like growth factor; IL: interleukin; MMP: matrix metalloproteinase; OA: osteoarthritis; PBS: phosphate-buffered saline; PCNA: proliferating cell nuclear antigen; PG: prostaglandin; PLGA: polylactic-co-glycolic acid; SD: standard deviation; TNF: tumor necrosis factor.

Acknowledgements

We are grateful to Tomohisa Kato, Akira Nasu, Takashi Kasahara, Kazuo Hayakawa, Kyosuke Kobayashi, Michiko Ueda, Sakura Tamaki, and Yukiko Kobayashi for their assistance. This work was partially supported by Grants-in-aid for Scientific Research from the Japan Society for the Promotion of Science, from the Ministry of Education, Culture, Sports, Science, and Technology, and from the Ministry of Health, Labor, and Welfare.

Author details

[1]Department of Tissue Regeneration, Institute for Frontier Medical Sciences, Kyoto University, 53 Kawahara-cho, Shogoin, Sakyo-ku, Kyoto 606-8507, Japan. [2]Department of Orthopaedic Surgery, Graduate School of Medicine, Kyoto University, 54 Kawahara-cho, Shogoin, Sakyo-ku, Kyoto 606-8507, Japan. [3]Department of Orthopaedic Surgery, Graduate School of Medical Sciences, Nagoya City University, Nagoya, Japan. [4]Department of Physical Therapy, Human Health Sciences, Graduate School of Medicine, Kyoto University, 53 Kawahara-cho, Shogoin, Sakyo-ku, Kyoto 606-8507, Japan. [5]Ono

Pharmaceutical Co. Ltd.,3-1-1 Sakurai, Shimamoto-cho, Mishima-gun, Osaka 618-8585, Japan. [6]Center for iPS Cell Research and Application, Kyoto University, 53 Kawahara-cho, Shogoin, Sakyo-ku, Kyoto 606-8507, Japan.

Authors' contributions

HM performed animal experiments, carried out analysis and interpretation of the data, and drafted the manuscript. TA conceived this study, designed the study, carried out analysis and interpretation of the data, and drafted the manuscript. MF and JY performed animal experiments and carried out analysis of the data. KI performed animal experiments. TM was the chief investigator in the development of materials, and conceived this study. TK designed and performed animal experiments. SF performed animal experiments and obtained samples from animals. HS was responsible for providing materials. NA was responsible for the development of drug delivery system. TO carried out administrative and financial support and helped to draft the manuscript. TN carried out administrative and financial support and helped to draft the manuscript. JT conceived this study, provided financial support, designed experiments, interpreted the data, and drafted the manuscript. All authors have read and approaved the manuscript for publication.

Competing interests

Takayuki Maruyama, Toshiya Kanaji, Shinsei Fujimura, Hikaru Sugihara, and Akio Nishiura are employees of Ono Pharmaceutical Co. Ltd. All other authors have no conflicts of interest.

Received: 19 January 2011 Revised: 28 June 2011
Accepted: 14 September 2011 Published: 14 September 2011

References

1. Peat G, McCarney R, Croft P: **Knee pain and osteoarthritis in older adults: a review of community burden and current use of primary health care.** *Ann Rheum Dis* 2001, **60**:91-97.
2. Buckwalter JA, Saltzman C, Brown T: **The impact of osteoarthritis: implications for research.** *Clin Orthop Relat Res* 2004, **427 Suppl**:S6-15.
3. Goldring SR, Goldring MB: **The role of cytokines in cartilage matrix degeneration in osteoarthritis.** *Clin Orthop Relat Res* 2004, **427 Suppl**: S27-36.
4. Goldring MB, Goldring SR: **Osteoarthritis.** *J Cell Physiol* 2007, **213**:626-634.
5. Billinghurst RC, Dahlberg L, Ionescu M, Reiner A, Bourne R, Rorabeck C, Mitchell P, Hambor J, Diekmann O, Tschesche H, Chen J, Van Wart H, Poole AR: **Enhanced cleavage of type II collagen by collagenases in osteoarthritic articular cartilage.** *J Clin Invest* 1997, **99**:1534-1545.
6. Neuhold LA, Killar L, Zhao W, Sung ML, Warner L, Kulik J, Turner J, Wu W, Billinghurst C, Meijers T, Poole AR, Babij P, DeGennaro LJ: **Postnatal expression in hyaline cartilage of constitutively active human collagenase-3 (MMP-13) induces osteoarthritis in mice.** *J Clin Invest* 2001, **107**:35-44.
7. Hu Y, Xiang JS, DiGrandi MJ, Du X, Ipek M, Laakso LM, Li J, Li W, Rush TS, Schmid J, Skotnicki JS, Tam S, Thomason JR, Wang Q, Levin JI: **Potent, selective, and orally bioavailable matrix metalloproteinase-13 inhibitors for the treatment of osteoarthritis.** *Bioorg Med Chem* 2005, **13**:6629-6644.
8. Narumiya S, Sugimoto Y, Ushikubi F: **Prostanoid receptors: structures, properties, and functions.** *Physiol Rev* 1999, **79**:1193-1226.
9. Laufer S: **Role of eicosanoids in structural degradation in osteoarthritis.** *Curr Opin Rheumatol* 2003, **15**:623-627.
10. Martel-Pelletier J, Pelletier JP, Fahmi H: **Cyclooxygenase-2 and prostaglandins in articular tissues.** *Semin Arthritis Rheum* 2003, **33**:155-167.
11. Bunning RA, Russell RG: **The effect of tumor necrosis factor alpha and gamma-interferon on the resorption of human articular cartilage and on the production of prostaglandin E and of caseinase activity by human articular chondrocytes.** *Arthritis Rheum* 1989, **32**:780-784.
12. Lippiello L, Yamamoto K, Robinson D, Mankin HJ: **Involvement of prostaglandins from rheumatoid synovium in inhibition of articular cartilage metabolism.** *Arthritis Rheum* 1978, **21**:909-917.
13. Li X, Ellman M, Muddasani P, Wang JH, Cs-Szabo G, van Wijnen AJ, Im HJ: **Prostaglandin E2 and its cognate EP receptors control human adult articular cartilage homeostasis and are linked to the pathophysiology of osteoarthritis.** *Arthritis Rheum* 2009, **60**:513-523.
14. Riquet FB, Lai WF, Birkhead JR, Suen LF, Karsenty G, Goldring MB: **Suppression of type I collagen gene expression by prostaglandins in fibroblasts is mediated at the transcriptional level.** *Mol Med* 2000, **6**:705-719.
15. Miyamoto M, Ito H, Mukai S, Kobayashi T, Yamamoto H, Kobayashi M, Maruyama T, Akiyama H, Nakamura T: **Simultaneous stimulation of EP2 and EP4 is essential to the effect of prostaglandin E2 in chondrocyte differentiation.** *Osteoarthritis Cartilage* 2003, **11**:644-652.
16. Di Battista JA, Dore S, Morin N, He Y, Pelletier JP, Martel-Pelletier J: **Prostaglandin E2 stimulates insulin-like growth factor binding protein-4 expression and synthesis in cultured human articular chondrocytes: possible mediation by Ca(++)-calmodulin regulated processes.** *J Cell Biochem* 1997, **65**:408-419.
17. Lowe GN, Fu YH, McDougall S, Polendo R, Williams A, Benya PD, Hahn TJ: **Effects of prostaglandins on deoxyribonucleic acid and aggrecan synthesis in the RCJ 3.1C5.18 chondrocyte cell line: role of second messengers.** *Endocrinology* 1996, **137**:2208-2216.
18. Aoyama T, Liang B, Okamoto T, Matsusaki T, Nishijo K, Ishibe T, Yasura K, Nagayama S, Nakayama T, Nakamura T, Toguchida J: **PGE2 signal through EP2 promotes the growth of articular chondrocytes.** *J Bone Miner Res* 2005, **20**:377-389.
19. Otsuka S, Aoyama T, Furu M, Ito K, Jin Y, Nasu A, Fukiage K, Kohno Y, Maruyama T, Kanaji T, Nishiura A, Sugihara H, Fujimura S, Otsuka T, Nakamura T, Toguchida J: **PGE2 signal via EP2 receptors evoked by a selective agonist enhances regeneration of injured articular cartilage.** *Osteoarthritis Cartilage* 2009, **17**:529-538.
20. Tani K, Naganawa A, Ishida A, Egashira H, Sagawa K, Harada H, Ogawa M, Maruyama T, Ohuchida S, Nakai H, Kondo K, Toda M: **Design and synthesis of a highly selective EP2-receptor agonist.** *Bioorg Med Chem Lett* 2001, **11**:2025-2028.
21. Okada H: **One- and three-month release injectable microspheres of the LH-RH superagonist leuprorelin acetate.** *Adv Drug Deliv Rev* 1997, **28**:43-70.
22. Park SR, Park SH, Jang KW, Cho HS, Cui JH, An HJ, Choi MJ, Chung SI, Min BH: **The effect of sonication on simulated osteoarthritis. Part II: alleviation of osteoarthritis pathogenesis by 1 MHz ultrasound with simultaneous hyaluronate injection.** *Ultrasound Med Biol* 2005, **31**:1559-1566.
23. Sakakibara Y, Miura T, Iwata H, Kikuchi T, Yamaguchi T, Yoshimi T, Itoh H: **Effect of high-molecular-weight sodium hyaluronate on immobilized rabbit knee.** *Clin Orthop Relat Res* 1994, 282-292.
24. Mankin HJ, Dorfman H, Lippiello L, Zarins A: **Biochemical and metabolic abnormalities in articular cartilage from osteo-arthritic human hips. II. Correlation of morphology with biochemical and metabolic data.** *J Bone Joint Surg Am* 1971, **53**:523-537.
25. Noguchi K, Maeda M, Ruwanpura SM, Ishikawa I: **Prostaglandin E2 (PGE2) downregulates interleukin (IL)-1alpha-induced IL-6 production via EP2/EP4 subtypes of PGE2 receptors in human periodontal ligament cells.** *Oral Dis* 2005, **11**:157-162.
26. Noguchi K, Shitashige M, Endo H, Kondo H, Ishikawa I: **Binary regulation of interleukin (IL)-6 production by EP1 and EP2/EP4 subtypes of PGE2 receptors in IL-1beta-stimulated human gingival fibroblasts.** *J Periodontal Res* 2002, **37**:29-36.
27. Tchetina EV, Di Battista JA, Zukor DJ, Antoniou J, Poole AR: **Prostaglandin PGE2 at very low concentrations suppresses collagen cleavage in cultured human osteoarthritic articular cartilage: this involves a decrease in expression of proinflammatory genes, collagenases and COL10A1, a gene linked to chondrocyte hypertrophy.** *Arthritis Res Ther* 2007, **9**:R75.
28. Sato T, Konomi K, Fujii R, Aono H, Aratani S, Yagishita N, Araya N, Yudoh K, Beppu M, Yamano Y, Nishioka K, Nakajima T: **Prostaglandin EP2 receptor signalling inhibits the expression of matrix metalloproteinase 13 in human osteoarthritic chondrocytes.** *Ann Rheum Dis* 2011, **70**:221-226.
29. Rashad S, Low F, Revell P, Hemingway A, Rainsford K, Walker F: **Effect of non-steroidal anti-inflammatory drugs on course of osteoarthritis.** *Lancet* 1989, **2**:1149.
30. Reijman M, Bierma-Zeinstra SM, Pols HA, Koes BW, Stricker BH, Hazes JM: **Is there an association between the use of different types of nonsteroidal antiinflammatory drugs and radiologic progression of osteoarthritis? The Rotterdam Study.** *Arthritis Rheum* 2005, **52**:3137-3142.
31. Shirai T, Kobayashi M, Nishitani K, Satake T, Kuroki H, Nakagawa Y, Nakamura T: **Chondroprotective effect of alendronate in a rabbit model of osteoarthritis.** *J Orthop Res* 2011, **29**:1572-7.
32. Burrage PS, Mix KS, Brinckerhoff CE: **Matrix metalloproteinases: role in arthritis.** *Front Biosci* 2006, **11**:529-543.

33. Nishitani K, Ito H, Hiramitsu T, Tsutsumi R, Tanida S, Kitaori T, Yoshitomi H, Kobayashi M, Nakamura T: **PGE2 inhibits MMP expression by suppressing MKK4-JNK MAP kinase-c-JUN pathway via EP4 in human articular chondrocytes.** *J Cell Biochem* 2010, **109**:425-433.
34. Pillinger MH, Rosenthal PB, Tolani SN, Apsel B, Dinsell V, Greenberg J, Chan ES, Gomez PF, Abramson SB: **Cyclooxygenase-2-derived E prostaglandins down-regulate matrix metalloproteinase-1 expression in fibroblast-like synoviocytes via inhibition of extracellular signal-regulated kinase activation.** *J Immunol* 2003, **171**:6080-6089.
35. Gosset M, Pigenet A, Salvat C, Berenbaum F, Jacques C: **Inhibition of matrix metalloproteinase-3 and -13 synthesis induced by IL-1beta in chondrocytes from mice lacking microsomal prostaglandin E synthase-1.** *J Immunol* 2010, **185**:6244-6252.
36. Clark CA, Li TF, Kim KO, Drissi H, Zuscik MJ, Zhang X, O'Keefe RJ: **Prostaglandin E2 inhibits BMP signaling and delays chondrocyte maturation.** *J Orthop Res* 2009, **27**:785-792.
37. Bau B, Gebhard PM, Haag J, Knorr T, Bartnik E, Aigner T: **Relative messenger RNA expression profiling of collagenases and aggrecanases in human articular chondrocytes in vivo and in vitro.** *Arthritis Rheum* 2002, **46**:2648-2657.
38. Kevorkian L, Young DA, Darrah C, Donell ST, Shepstone L, Porter S, Brockbank SM, Edwards DR, Parker AE, Clark IM: **Expression profiling of metalloproteinases and their inhibitors in cartilage.** *Arthritis Rheum* 2004, **50**:131-141.
39. Klatt AR, Paul-Klausch B, Klinger G, Kuhn G, Renno JH, Banerjee M, Malchau G, Wielckens K: **A critical role for collagen II in cartilage matrix degradation: collagen II induces pro-inflammatory cytokines and MMPs in primary human chondrocytes.** *J Orthop Res* 2009, **27**:65-70.

doi:10.1186/ar3460
Cite this article as: Mitsui *et al.*: Prostaglandin E2 receptor type 2-selective agonist prevents the degeneration of articular cartilage in rabbit knees with traumatic instability. *Arthritis Research & Therapy* 2011 **13**:R146.

THE JOURNAL OF BIOLOGICAL CHEMISTRY VOL. 286, NO. 10, pp. 7947–7957, March 11, 2011

The Endoplasmic Reticulum Stress Sensor, ATF6α, Protects against Neurotoxin-induced Dopaminergic Neuronal Death*[S]

Received for publication, June 22, 2010, and in revised form, October 17, 2010 Published, JBC Papers in Press, December 3, 2010, DOI 10.1074/jbc.M110.156430

Naohiro Egawa[‡§], Keisuke Yamamoto[¶‖], Haruhisa Inoue[**], Rie Hikawa[‡§], Katsunori Nishi[‡‡], Kazutoshi Mori[§¶], and Ryosuke Takahashi[‡§1]

From the [‡]Department of Neurology, Graduate School of Medicine, Kyoto University, Kyoto 606-8507, Japan, [§]Core Research for Evolutional Science and Technology (CREST), Japan Science and Technology Corporation, Japan, the [¶]Department of Biophysics, Graduate School of Science, Kyoto University, Kyoto 606-8502, Japan, the [‖]Institute of Genome Research, Tokushima University, Tokushima 770-8503, Japan, the [**]Center for iPS Cell Research and Application (CiRA), Kyoto University, Kyoto 606-8507, Japan, and the [‡‡]Tokyo Metropolitan Institute for Neuroscience, Tokyo 183-8526, Japan

Oxidative stress and endoplasmic reticulum (ER) stress are thought to contribute to the pathogenesis of various neurodegenerative diseases including Parkinson disease (PD), however, the relationship between these stresses remains unclear. ATF6α is an ER-membrane-bound transcription factor that is activated by protein misfolding in the ER and functions as a critical regulator of ER quality control proteins in mammalian cells. The goal of this study was to explore the cause-effect relationship between oxidative stress and ER stress in the pathogenesis of neurotoxin-induced model of PD. 1-Methyl-4-phenyl-1,2,3,6-tetrahydropyridine (MPTP), a dopaminergic neurotoxin known to produce oxidative stress, activated ATF6α and increased ER chaperones and ER-associated degradation (ERAD) component in dopaminergic neurons. Importantly, MPTP induced formation of ubiquitin- immunopositive inclusions and loss of dopaminergic neurons more prominently in mice deficient in ATF6α than in wild-type mice. Cultured cell experiments revealed that 1-methyl-4-phenylpyridinium (MPP^+)-induced oxidative stress not only promoted phosphorylation of p38 mitogen-activated protein kinase (p38MAPK) but also enhanced interaction between phosphorylated p38MAPK and ATF6α, leading to increment in transcriptional activator activity of ATF6α. Thus, our results revealed a link between oxidative stress and ER stress by showing the importance of ATF6α in the protection of the dopaminergic neurons from MPTP that occurs through oxidative stress-induced activation of ATF6α and p38MAPK-mediated enhancement of ATF6α transcriptional activity.

Parkinson disease (PD)[2] is characterized pathologically by progressive and selective loss of dopaminergic neurons in the substantia nigra pars compacta (SNc). Recent studies have suggested some pathogenetic mechanisms of PD, including mitochondrial dysfunction (1), oxidative stress induced by dopamine metabolites, and endoplasmic reticulum (ER) stress induced by the accumulation of unfolded proteins (2–4). Dopaminergic neuron loss is often accompanied by formation of intraneuronal inclusion bodies termed Lewy bodies whose major constituent is α-synuclein (5), suggesting the pathogenetic role of unfolded protein accumulation and aggregation.

The unfolded protein response (UPR) is a homeostatic signaling pathway designed to cope with the accumulation of unfolded proteins in the ER lumen. In mammals, the UPR utilize three types of sensor proteins, PERK, IRE1α, and ATF6α, which detect protein-misfolding stress in the ER and initiate ER-to-nucleus signaling cascades to maintain the homeostasis of protein quality control system (6). ATF6 is a type 2 transmembrane protein; the C-terminal region is located in the ER, whereas the N-terminal region is located in the cytosolic side. ATF6 consists of two subtypes, ATF6α and ATF6β. ATF6α or ATF6β single knock-out mice normally develops but mice deficient in both subtypes of ATF6 genes showed embryonic lethal (7, 8). Upon ER stress the N-terminal fragment of ATF6α designated pATF6α(N) is cleaved from the parent protein designated pATF6α(P) and transported into the nucleus, where it binds to cis-acting ER stress response element (ERSE) and UPR element (UPRE), and up-regulates major ER chaperones and ER-associated degradation (ERAD) components (9–14).

1-Methyl-4-phenyl-1,2,3,6-tetrahydropyridine (MPTP) is converted into 1-methyl-4- phenylpyridinium (MPP^+) in astrocytes and taken up by dopaminergic neurons through the dopamine transporter (DAT). MPP^+ interferes with the mitochondrial complex-1, generates reactive oxygen species (ROS) and selectively damages dopaminergic neurons (15). Dopamine itself is also a highly-reactive molecule and naturally metabolized to produce ROS including hydrogen peroxide (H_2O_2) via the monoamine oxidase pathway (16). Dopamine-induced ROS promotes phosphorylation of p38 mitogen-activated protein kinase (p38MAPK) (17). MPTP activates p38MAPK pathway in the dopaminergic neuron (18). Other

* This study was supported in part by a grant-in-aid for scientific research on Priority Areas-Research on Pathomechanisms of Brain Disorders from the Ministry of Education, Culture, Sports, Science and Technology of Japan and a Grant-in-aid from the Ministry of Health, Labor, and Welfare of Japan.

[S] The on-line version of this article (available at http://www.jbc.org) contains supplemental Table S1 and Figs. S1–S3.

[1] To whom correspondence should be addressed: Dept. of Neurology, Kyoto University Graduate School of Medicine, 54 Shogoin-Kawahara-cho, Sakyo-ku, Kyoto 606-8507, Japan. Tel.: 81-75-751-3770; Fax: 81-75-761-9780; E-mail: ryosuket@kuhp.kyoto-u.ac.jp.

[2] The abbreviations used are: PD, Parkinson disease; ER, endoplasmic reticulum; MPTP, 1-methyl-4-phenyl-1,2,3,6-tetrahydropyridine; ERAD, ER-associated degradation; UPR, unfolded protein response; MPP^+, 1-methyl-4-phenylpyridinium.

oxidative neurotoxins such as rotenone and 6-hydroxydopamine (6-OHDA) also enhance the phosphorylation of p38MAPK (19, 20). Interestingly, it was previously reported that phosphorylated p38MAPK can regulate ATF6α function via phosphorylation (21), suggesting the possibility that oxidative stress and ER stress intersect at the level of p38MAPK and ATF6α.

Based on these data, the goal of the present study was to explore the cause-effect relationship between oxidative stress and ER stress in the pathogenesis of PD using ATF6α wild-type (WT) and knock-out (KO) mice treated with MPTP that causes oxidative stress and damages dopaminergic neurons.

EXPERIMENTAL PROCEDURES

Animal and MPTP Treatment—ATF6α knock-out (KO) mice were generated by gene targeting techniques as previously described (7). Groups of male ATF6α KO mice and wild-type (WT) littermate controls were injected intraperitoneal with 20 mg/kg of MPTP hydrochloride (Sigma-Aldrich) four times at 2 h intervals on the same day ($n = 10$ for each group). The mice were decapitated 5 days after injection for the subsequent analysis. All surgical procedures were performed according to the rules set forth by the Ethics Committee of Kyoto University.

Quantitative Real-time PCR—The mouse central nervous system (CNS) was dissected into the cerebral cortex, the brainstem, the hippocampus, the striatum, the midbrain, the cerebellum, the olfactory bulb, and the thalamus. Total RNA was isolated from the various parts of the CNS using the RNeasy Kit (Qiagen, Valencia CA) after homogenization (POLYTRON PT10–35). The first strand of cDNA was synthesized from 1 μg of total RNA using the PrimeScript RT Reagent Kit (Takara Bio, Shiga). Real-time PCR was performed using the LightCycler SYBR Green Master Kit and LightCycler 480 program (Roche) according to the manufacturer's protocol. The sequences of the primers used were listed in the supplemental Table S1. Values were normalized and expressed relative to GAPDH values.

Immunoblotting—Each part of the dissected CNS tissue was weighed and homogenized (POLYTRON PT10–35) in 1 ml/g of ice-cold buffer (50 mM Tris(pH7.5), 5 mM EDTA and 120 mM NaCl, 1% Triton X-100) containing protease inhibitor and phosphatase inhibitor mixture. Samples were centrifuged at 1,000 × *g* for 5 min, where the supernatant was collected for the additional centrifugation and the resulting pellet was dissolved in 2% SDS buffer for nuclear fraction. The supernatant was centrifuged at 165,000 × *g* for 60 min. The supernatant was prepared for cytosolic fraction, and the resulting pellet was dissolved in 2% SDS buffer as the ER and vesicle fraction. SH-SY5Y cells, HEK293T cells, ATF6α WT and ATF6α KO mouse embryonic fibroblasts (MEFs) were lysed in lysis buffer containing 1% Triton X-100 or 2% SDS buffer containing protease inhibitor and phosphatase inhibitor mixture. 20 or 30 μg of protein for each sample was separated by SDS-PAGE and electroblotted onto PDGF membrane (Immunopore). Immunoblotting analysis was carried out using an enhanced chemiluminescence Western blotting detection system kit (Amersham Biosciences). Rabbit anti-ATF6α polyclonal antibody was prepared as previously described (13). Mouse anti-BiP antibody was purchased from BD Biosciences (San Diego, CA). Rat anti-GRP94 antibody was purchased from Stressgen (Ann Arbor, MI). Rabbit anti-Derlin-3 antibody was purchased from Sigma-Aldrich. β-Actin antibody, anti-p38MAPK antibody, anti-phosho-p38MAPK (p-p38MAPK) antibody and anti-IRE1α antibody were obtained from Cell Signaling (Boston, MA). Rabbit anti-DAT antibody and mouse anti-tyrosine hydroxylase (TH) antibody were purchased from Millipore (Billerica, MA). Rabbit anti-ubiquitin antibody was purchased from DAKO (Glostrup, Denmark). Goat anti-PERK and rabbit anti-phospho-PERK antibody were obtained from Santa Cruz Biotechnology.

Immunohistochemistry—Mice were injected with pentobarbital and perfused transcardially with PBS, followed by 4% paraformaldehyde in PBS. Mice were decapitated, and their brains were removed and immersed in 4% paraformaldehyde in PBS for fixation. Serial coronal sections at 20-μm thickness were collected on slides. Deparaffinized sections were rinsed with PBS containing 0.1% Triton X-100 and then immersed in 0.3% H_2O_2 for 30 min. Sections were stained with primary antibodies against TH (mouse monoclonal; Millipore), BiP (IMGENEX, San Diego, CA) or ubiquitin (DAKO) or p-p38MAPK (Cell Signaling) in 10% normal serum overnight at 4 °C. After washing three times in PBST, the sections were stained with biotinylated secondary antibodies (Vector Laboratories, Burlingame, CA), using the standard avidin-biotin peroxidase method (Elite standard kit SK6100; Vector Laboratories, Burlingame, CA). SH-SY5Y cells, HEK293T cells and primary cultured dopaminergic neurons cultured in 4-well tissue culture chamber were fixed with 10% formaldehyde for 60 min on ice followed by acetone treatment for 5 min. They were then permeabilized with PBS containing 0.2% Triton X-100 for 10 min at room temperature and blocked with 10% goat serum for 30 min. They were then exposed to primary antibody overnight at 4 °C for indirect immunofluorescence. Anti-p38MAPK antibody and anti-p-p38MAPK were diluted 25-fold and 100-fold, respectively, with PBS containing 1% BSA before use. For immunofluorescence, primary antibodies were visualized by incubation for 2 h at room temperature with Alexa Fluor488- and Alexa Fluor546-conjugated secondary antibodies (Molecular Probes), followed by confocal laser scanning fluorescence microscopy using an LSM510 microscope(Carl Zeiss, Thornwood, NY).

TH-positive Cell and Ubiquitin-positive Inclusion Counting—Total numbers of TH-positive neurons in the substantia nigra pars compacta (SNc) and ubiquitin-positive inclusions in the striatum were determined using an unbiased optical fractionator method (Stereoinvestigator, MicroBrightField) as previously described with minor modification (4). Three independent sets of immunostained serial sections (sampled as every sixth coronal section throughout the entire range of SNc or the striatum) were analyzed for each animal. Total positive number for each sample was determined in triplicate by the Stereoinvestigator program to obtain averaged values. Location of SNc and the striatum was identified according to established anatomical landmarks (Paxinos mouse brain atlas).

Measurements of Striatal Catecholamines (HPLC)—Tissues dopamine and metabolites were measured according to previously published methods (4).

Plasmids, Cell Culture, Reagent, and Transfection—Various vectors, including pCMVfull-EGFP-ATF6α (also known as green fluorescent protein (GFP)-ATF6α fusion gene) (11), pGL3-GRP78 (−132)-Luc carrying the human BiP promoter, pGL3–5×UPRE-luc, pDNA3.1 (+)-N-terminal fragment of ATF6α (1–373) and a dominant-negative form of ATF6α (171–373) were prepared as previously (13, 14). Flag-p38MAPK was kindly provided by Dr. Katsuji Yoshioka (Kanazawa Univ.) ATF6α WT/KO primary cultured dopaminergic neurons were prepared as shown under "Primary culture." ATF6α WT/KO MEFs were obtained as previously described (7). SH-SY5Y cells were cultured in DMEM supplemented with 10% fetal bovine serum, NEAA (Invitrogen) at 37 °C in a humidified 5% CO_2/95% air atmosphere. HEK293T cells and ATF6α WT/KO MEFs were cultured in DMEM supplemented with 10% fetal bovine serum, 2 mM glutamine, and antibiotics (100 units/ml penicillin and 100 μg/ml streptomycin). Transfection was performed using Lipofectamine 2000 (Invitrogen, Carlsbad, CA) according to each manufacturer's protocol. 1-Methyl-4-phenylpyridinium iodide (MPP^+) was purchased from Sigma-Aldrich. SB203585 were purchased from Calbiochem (San Diego, CA). SHSY5Y cells and ATF6α WT/KO primary cultured dopaminergic neurons were treated with 1 mM MPP^+ for indicated times in the presence or absence of 5 μM SB203585. ATF6α WT/KO MEFs and HEK293T cells were plated in 6-well plates and treated with 50 μM hydroxyl peroxide (H_2O_2) (Nakalai Tesque, Kyoto) in the presence or absence of 5 μM SB203585.

Primary Culture—Mesencephalic and striatal cells were prepared from embryonic day 15 ATF6α WT/KO mice. Both the midbrain and the striatum were mechanically dissected in Neurobasal medium (Invitrogen). The tissues were dissociated with 0.25% trypsin at room temperature for 15 min. The cells were suspended in DMEM supplemented with 10% fetal bovine serum and NEAA and then collected by centrifugation (1000 × *g*, 3 min). The cells were resuspended in Neurobasal medium supplemented with B-27(minus Anti-Oxidants) (Invitrogen) and 0.5 mM glutamine at a concentration of 1million cells/ml, and plated at a density of 0.5 million cells per well into 24 well plate previously coated with poly-L-Lysin (Sigma-Aldrich). One week after plating, the cells were used for reporter assay or immunohistochemistry.

Reporter Assay—SH-SY5Y cells, HEK293T cells and ATF6α WT/KO primary cultured dopaminergic neurons were transiently transfected with pGL3–5×UPRE or pGL3-BiP (-132) along with pRL-SV40 (Promega, Madison, WI) using Lipofectamine 2000 (Invitrogen). After 48 h, the cells were treated with 1 mM MPP^+ for 24 h or 50 μM H_2O_2 for 1 h in the presence or absence of 5 μM SB203585. Luciferase expression was measured in triplicate using a dual luciferase reporter assay system (Promega) on Fluoroskan Ascent FL (Thermo, Waltham, MA). Relative activity was defined as the ratio firefly luciferase activity to *Renilla* luciferase activity to normalize for transfection efficiency.

Immunoprecipitation—After being washed with PBS, SH-SY5Y cells and HEK293T cells cultured in a 6-well plate dish were solubilized for 30 min on ice in 200 μl of RIPA buffer (50 mM Tris-HCl, 150 mM NaCl, 1 mM EDTA, 1% Triton X-100, 0.1% SDS, and 0.1% sodium deoxycholate) with a protease inhibitor mixture and a phosphatase inhibitor. Insoluble fraction was collected by centrifugation (1000 × *g*, 3 min), defined as nuclear fraction, and lysed in SDS lysis solution (50 mM Tris-HCl, 10 mM EDTA, 1% SDS) including phosphatase inhibitor. Soluble lysates were incubated overnight with ANTI-FLAG M2 Affinity gel (Sigma-Aldrich). Lysates from nuclear fraction were diluted to 10% by dilution buffer (50 mM Tris-HCl, 167 mM NaCl, 1.1% Triton X-100, and 0.11% sodium deoxycholate) including phosphatase inhibitor and then incubated for overnight by G-Sepharose bound to anti-phospho-p38MAPK antibody(Cell Signaling). Sepharose beads were collected by brief centrifugation and washed with TBS buffer (50 mM Tris-HCl, 150 mM NaCl, pH7.4) three times. Immunoprecipitated material was eluted by boiling for 3 min in 2× sample buffer (125 mM Tris-HCl, pH 6.8, 4% SDS, 20% glycerol, 0.004% BPB).

Chromatin Immunoprecipitation (ChIP) Assay—SH-SY5Y cells were grown to 80% confluence in 6-cm plates and then treated with 1 mM MPP^+ for 24 h and protein-DNA cross-linking was initiated by adding formaldehyde to the cell culture to a final concentration of 1% and stopped at 15 min by adding 1.5 M glycine to a final concentration of 0.15 M. The cells were lysed in RIPA buffer including a protease inhibitor mixture and a phosphatase inhibitor. Insoluble fraction was collected by centrifugation (1000 × *g*, 3 min), defined as nuclear fraction, lysed in SDS lysis solution (50 mM Tris-HCl, 10 mM EDTA, 1% SDS) including phosphatase inhibitor and sonicated for 25 min using Bioruptor (UCD-200TM, COSMO BIO) (Sonication pulse was performed by power high, ON 30 s, OFF 60 s). Diluted to 10% by ChIP dilution buffer (50 mM Tris-HCl, 167 mM NaCl, 1.1% Triton X-100, and 0.11% sodium deoxycholate) including phosphatase inhibitor, lysates were incubated for overnight by G-Sepharose bound to anti-phospho-p38MAPK antibody. Sepharose beads were collected by brief centrifugation, washed with RIPA buffer three times and suspended with ChIP direct elution buffer (10 mM Tris-HCl, 300 mM NaCl, 5 mM EDTA, 0.5% SDS). Formaldehyde-induced cross linking was reversed (for overnight at 65 °C) and the DNA was purified by phenol-chloroform extraction and ethanol precipitation. Purified DNA was subjected to quantitative PCR by LightCycler 480 program.

Statistical Analysis—All values are presented as the mean ± S.D. Results were tested for significant differences using one-way ANOVA with the posthoc test or Student's *t* test. $p < 0.05$ was considered to represent significant difference. In figures, a single asterisk (*) indicates $p < 0.05$, and a double asterisk (**) indicates $p < 0.01$.

RESULTS

ATF6α Controls the Levels of ER Chaperones and ERAD Component in the Dopaminergic Neuron System in Vivo—To explore the physiological function of ATF6α *in vivo*, we first investigated where in the central nervous system ATF6α is

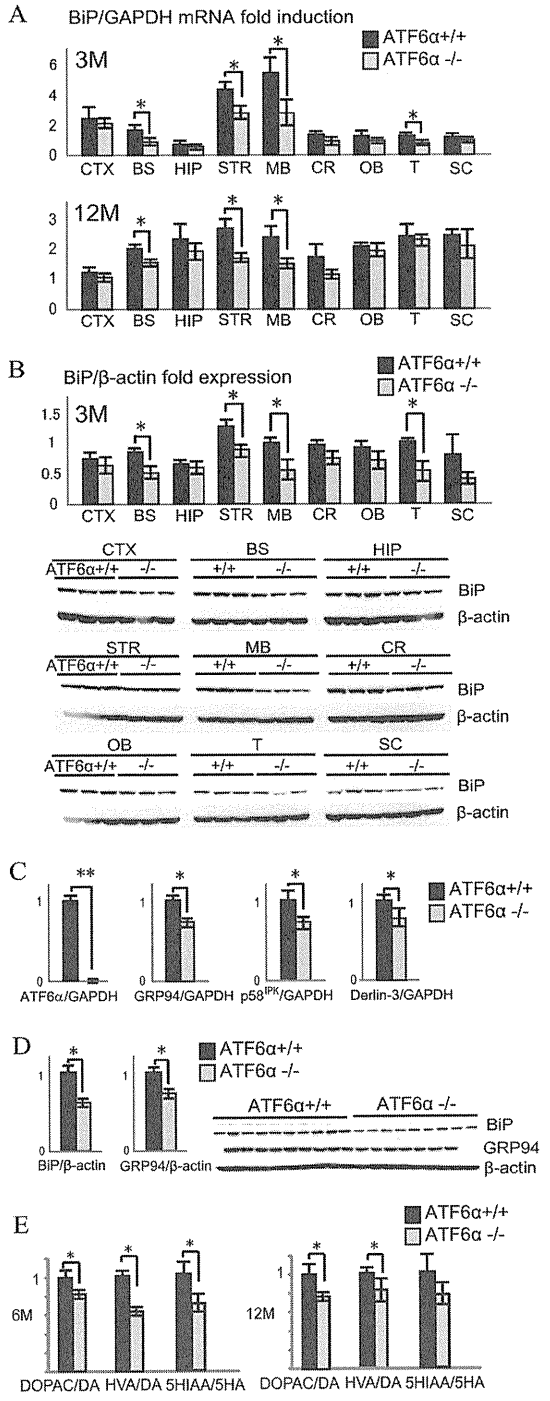

FIGURE 1. **ATF6α controls the levels of ER chaperones and ERAD component in the dopaminergic neuron system under physiological conditions *in vivo*.** *A*, ATF6α controls the mRNA levels of BiP in the brainstem, the midbrain and the striatum in mice brain *in vivo*. Total RNA was isolated from various sections of brain of 3 and 12-month-aged male ATF6α KO(−/−) mice and ATF6α WT(+/+) littermates and analyzed by quantitative real-time RT-PCR for detecting the level of BiP mRNA. ($n = 5$ for each group). Fold induction of mRNA level is defined relative to GAPDH mRNA level. Abbreviation: *CTX*, cerebral cortex; *BS*, brainstem; *HIP*, hippocampus; *STR*, striatum; *MB*, midbrain; *CR*, cerebellum; *OB*, olfactory bulb; *T*, thalamus; *SC*, spinal cord; 3 M, 3 months aged group; 12 M, 12-month-aged group. The *asterisk* indicates statistical significance (*, $p < 0.05$; **, $p < 0.01$). Each bar denotes the mean ± S.D. *B*, ATF6α controls the protein levels of BiP in the brainstem, the midbrain and the striatum in mice brain *in vivo*. The tissue lysates of 3-month-aged ATF6α KO mice and ATF6α WT littermate were subjected to Western blot analysis for detection of BiP and β-actin ($n = 5$). Each protein level was quantified using optical density and estimated relative to β-actin protein level. *C*, ATF6α controls the levels of GRP94, p58^{IPK}, and Derlin-3 in the midbrain *in vivo*. Quantitative real-time RT-PCR was performed from the midbrain samples of 12-month-aged ATF6α KO mice and ATF6α WT littermates using ATF6α, GRP94, p58^{IPK}, and Derlin-3 primers ($n = 5$ for each group). *D*, ATF6α controls the protein levels of BiP and GRP94 in the striatum *in vivo*. ($n = 7–10$). *E*, metabolisms of dopamine and serotonin were decreased in ATF6α KO mice as compared with ATF6α WT mice. Metabolisms of dopamine and serotonin were defined as the relative ratio of DOPAC or HVA to dopamine and 5HIAA to 5HA, respectively. The striatal levels of dopamine, serotonin, and their metabolites were measured by HPLC ($n = 8–10$ for each group). Abbreviations: *DA*, dopamine; *DOPAC*, 3,4-dihydroxyphenylacetic acid; *HVA*, homovanillic acid; *5HIAA*, 5-hydroxyindole acetic acid; *5HA*, 5-hydroxytryptamine; 6 M, 6-month-aged group; 12 M, 12-month-aged group.

activated under normal physiological conditions by using ATF6α WT or KO mice. Results of quantitative RT-PCR analysis demonstrated that mRNA level of the ER chaperone BiP was significantly lower in the brainstem, the midbrain and the striatum of ATF6α KO mice than those of ATF6α WT mice (Fig. 1*A*). Accordingly, the protein levels of BiP were also significantly lower in the brainstem, the midbrain and the striatum of ATF6α KO mice than those of ATF6α WT mice (Fig. 1*B*). Other ER stress sensor, IRE1α, sXBP1, and phosphorylated PERK (p-PERK, indicative of the activation status of another ER stress sensor molecule) are not different in various brain regions of ATF6α KO mice (supplemental Fig. S1*A*). The mRNA levels of other ER chaperone GRP94, cochaperone p58^{IPK}, and ERAD component, Derlin-3, in the midbrain were also significantly decreased in ATF6α KO mice when compared with age-matched ATF6α WT mice (Fig. 1*C*). The protein levels of GRP94 in the striatum were significantly decreased in ATF6α KO mice (Fig. 1*D*). HPLC analysis of the striatum demonstrated that the metabolisms of dopamine and serotonin were slightly but significantly decreased in ATF6α KO mice as compared with WT mice (Fig. 1*E*). Decreased protein levels were not general feature of ATF6α KO mice because the levels of some proteins involved in synaptic secretion or vesicular transport remained unchanged or rather increased in ATF6α KO mice as compared with WT mice (supplemental Fig. S1*B*). Importantly, tyrosine hydroxylase (TH) immunostaining of the midbrain revealed that there was no abnormality in the number and morphology of TH positive neurons in ATF6α KO mice when compared with WT littermates (supplemental Fig. S1, *C* and *D*). TH and DAT protein levels in the striatum of ATF6α KO mice were similar to those of WT littermates (supplemental Fig. S1*E*). Therefore, although ATF6α is not essential for the development and the survival of dopaminergic neurons, ATF6α up-regulates ER chaperones and ERAD component constitutively in dopaminergic neurons; dopaminergic neurons may experience ER stress under normal physiological conditions.

MPTP Up-regulates the Levels of ER Chaperones and ERAD Component by Activating ATF6α and Induces the Phosphorylation of p38MAPK in the Dopaminergic Neurons in Vivo—To investigate whether ATF6α plays an important role in dopaminergic cell death of neurotoxin-based PD models, we analyzed dopaminergic neurons of mice treated with MPTP. MPTP was intraperitoneally administered into 6-month-old

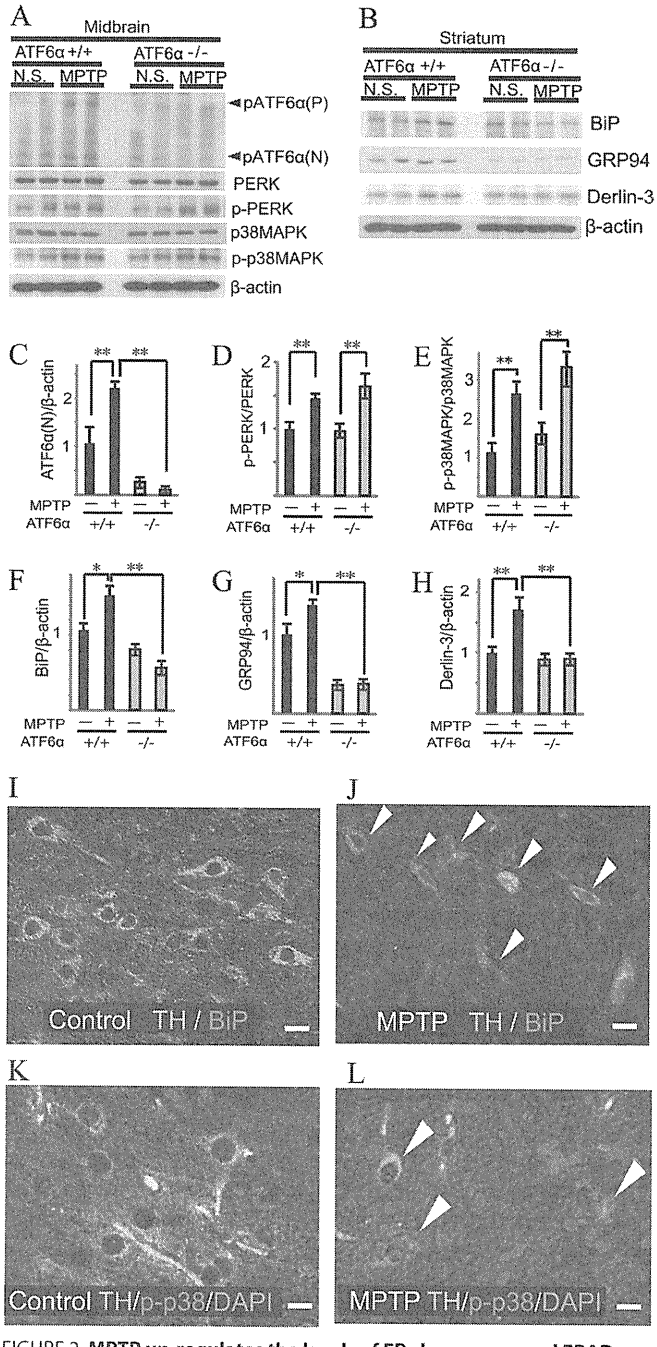

FIGURE 2. **MPTP up-regulates the levels of ER chaperones and ERAD component by activating ATF6α and induces the phosphorylation of p38 MAPK in dopaminergic neurons *in vivo*.** *A–H*, extracts of the midbrain or the striatum of ATF6α WT(+/+) and ATF6α KO(−/−) mice were prepared 5 days after intraperitoneal injection with either 20 mg/kg MPTP or normal saline four times every 2 h for Western blot analysis of ATF6α, PERK, p38MAPK, phospho-PERK (p-PERK), phospho-p38MAPK (p-p38MAPK), BiP, GRP94, Derlin-3, and β-actin ($n = 4$ for each group). The protein levels of p-PERK and p-p38MAPK were quantified using optical density and estimated relative to PERK or p38MAPK protein level, respectively. Other protein levels were estimated relative to β-actin protein level. Each bar denotes the mean ± S.D. MPTP induces ATF6α cleavage (*A* and *C*), phosphorylation of PERK (*A* and *D*) and p38MAPK activation (*A* and *E*) in the midbrain. MPTP up-regulates the levels of BiP (*B* and *F*), GRP94 (*B* and *G*), and Derlin-3 (*B* and *H*) in the striatum *in vivo*. Abbreviation: *N.S.* indicates normal saline injection as control. *I–L*, MPTP up-regulates the levels of BiP and p-p38MAPK in TH-positive neurons. The midbrains of ATF6α WT mice treated with MPTP or normal saline (Control) were stained using anti-TH (*I–L*, *green*), BiP (*I* and *J*, *red*), p-p38MAPK (*K* and *L*, *red*) antibodies, and DAPI (*K* and *L*, *blue*). They were visualized by Alexa Fluor 488- and Alexa Fluor 546-conjugated secondary antibodies and subjected to confocal fluorescence microscope analysis. *White arrowheads* in *J* and *L* indicate the TH-positive dopaminergic cells of MPTP-treated mice. Scale bars indicate 10 μm.

ATF6α KO mice and WT littermates. Western blot analysis with antibodies against ATF6α, PERK, p38MAPK, phosphorylated p38MAPK (p-p38MAPK), p-PERK, BiP, GRP94, and Derlin-3 was performed using midbrain and striatal extracts from WT or ATF6α KO mice challenged with MPTP. MPTP treatment induced phosphorylation of p38MAPK in the midbrain regardless of ATF6α genotype as expected (Fig. 2, *A* and *E*). Importantly, MPTP treatment not only increased the level of pATF6α (P), the precursor form of ATF6α, but also generated pATF6α (N), the active form produced as a result of the cleavage of pATF6α (P), in the midbrain of ATF6α WT mice (Fig. 2, *A* and *C*). The levels of ER chaperones, BiP and GPR94, and ERAD component, Derlin-3, were significantly increased in the striatum of MPTP-treated WT mice (Fig. 2, *B*, *F*, *G*, and *H*). In marked contrast, the induction of these ER chaperones and ERAD components was not observed in ATF6α KO mice even though MPTP increased phosphorylation of PERK regardless of ATF6α genotype (Fig. 2, *A* and *D*). To identify the cell types in which BiP was up-regulated, we performed double immunostaining for BiP in TH-positive dopaminergic neurons of the midbrain of WT mice. Dopaminergic neurons showed higher BiP expression level in MPTP-treated WT mice than untreated control mice (Fig. 2, *I* and *J*). Phosphorylated p38MAPK was detected in the nucleus of the dopaminergic neurons in the midbrain of MPTP-treated mice (Fig. 2, *K* and *L*) as previously reported (18). These data clearly indicate that MPTP somehow evokes ER stress and up-regulates the expression of ER chaperones and ERAD component by activating ATF6α in dopaminergic neurons *in vivo* in addition to previously known effect on the phosphorylation of p38MAPK. One possible cause for induction of ER stress by MPTP is production of ROS as we found that treatment of mouse embryonic fibroblasts (MEFs) derived from ATF6α WT mice with hydrogen peroxide, a representative ROS, triggered not only phosphorylation of p38MAPK but also cleavage of pATF6α(P) to produce pATF6α(N) (supplemental Fig. S2*A*).

ATF6α Protects against MPTP-induced Neurotoxicity in Vivo—We then asked whether ATF6α deletion and the sequential decline in the expression levels of ER chaperones and ERAD component have an impact on the ubiquitin proteasome system (UPS)-mediated protein degradation in dopaminergic neurons after MPTP treatment. Immunostaining of the striatum with antibody to ubiquitin revealed no difference in the striatum between ATF6α WT and KO mice under physiological conditions. However, upon stress with MPTP, the striatum of ATF6α KO mice showed much higher increase in the formation of clusters of ubiquitin-immunoreactive material than WT mice, suggesting that treatment with MPTP disturbed UPS more profoundly when the levels of ER chaperones and ERAD components were mitigated (Fig. 3, *A* and *B*). Next we assessed for neurotoxicity caused by treat-

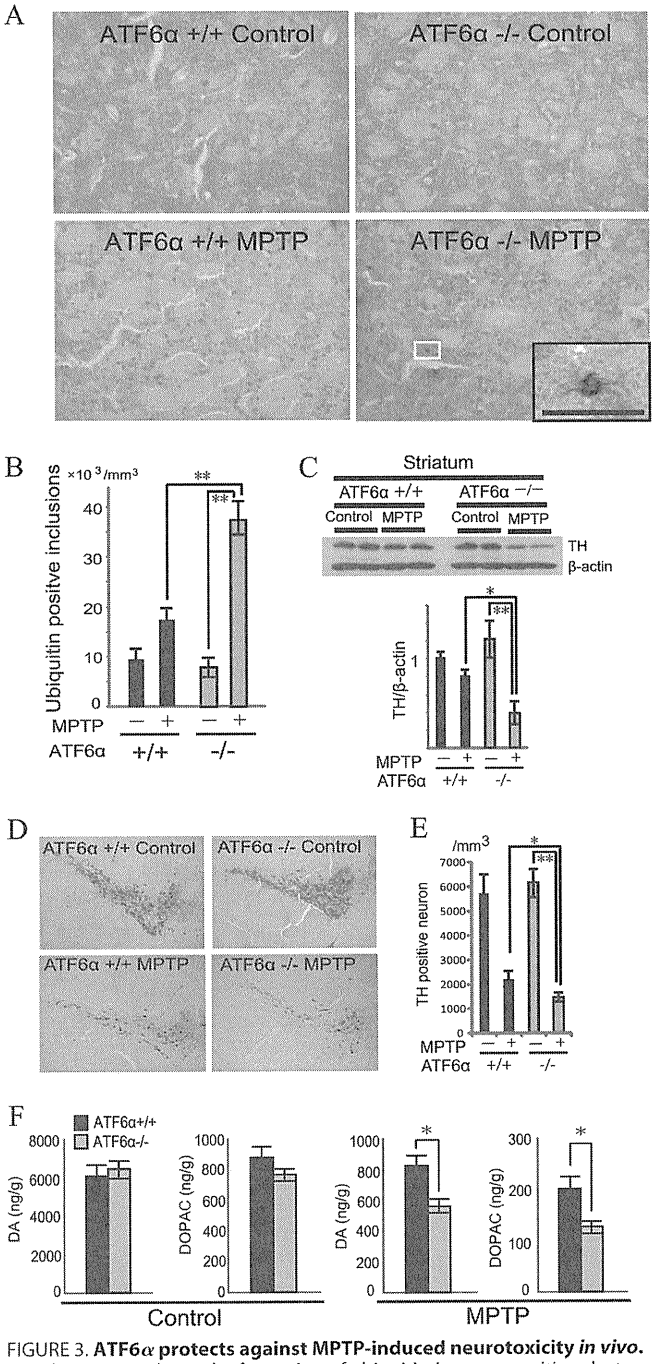

FIGURE 3. **ATF6α protects against MPTP-induced neurotoxicity *in vivo*.** *A* and *B*, MPTP induces the formation of ubiquitin-immunopositive clusters in the striatum of ATF6α KO(−/−) mice. *A*, representative images of ubiquitin-immunoreactive clusters in the striatum of ATF6α WT(+/+) and ATF6α KO mice treated with either 20 mg/kg MPTP or normal saline (Control) four times every 2 h. The *white box* marks the area enlarged in *lower right black box*. Scale bars indicate 50 μm. *B*, numbers of ubiquitin-immunoreactive inclusion per the volume of ROI in the striatum of individual mice were quantified by Stereoinvestigator and the density was compared among each indicated group. (n = 4 for each group). Each bar denotes the mean ± S.D. *C–F*, dopaminergic neurons of ATF6α KO mice are more vulnerable to MPTP neurotoxicity than ATF6α WT mice. *C*, extracts of the striatum of ATF6α WT and ATF6α KO mice with MPTP treatment or normal saline (Control) were subjected for Western blot analysis of TH and β-actin (n = 4 for each group). TH protein level was quantified using optical density and estimated relative to β-actin protein level. *D*, representative TH-immunostained images of the midbrain of ATF6α WT and ATF6α KO mice treated with normal saline (Control) or MPTP. *E*, TH-positive numbers in the midbrain SNc of ATF6α WT and ATF6α KO male littermates treated with MPTP or normal saline (n = 5 for each group). *F*, quantification of the striatal levels of dopamine and its metabolite DOPAC in ATF6α WT and ATF6α KO mice treated with either MPTP or normal saline (Control) (n = 5 for each group). Abbreviations: *DA*, dopamine; *DOPAC*, 3,4-dihydroxyphenylacetic acid.

ment with MPTP. Immunoblotting of the extracts from the striatum using TH antibody showed more remarkably decreased level of TH in ATF6α KO mice than in WT after treatment with MPTP, indicating that more dopaminergic terminal loss takes occurs in ATF6α KO mice (Fig. 3*C*). The number of TH-positive neurons in the SNc was significantly decreased in MPTP-treated ATF6α KO mice when compared with WT littermates (Fig. 3, *D* and *E*). These results were correlated with those of HPLC analysis, which showed significant decreases of dopamine and its metabolites, 3,4-dihydroxyphenylacetic acid (DOPAC), in the striatum of MPTP-treated ATF6α KO mice when compared with WT littermates (Fig. 3*F*). These results indicate that MPTP induces a larger loss of dopaminergic neurons and their terminals under ATF6α-deleted conditions and further suggest that ATF6α protects against MPTP-induced neurotoxicity.

Phosphorylated p38MAPK and Activated ATF6α Cooperate to Enhance the Expression Level of BiP in Dopaminergic Neurons Treated with MPP⁺—Next we investigated the possible cooperation between p38MAPK phosphorylated and ATF6α activated in MPTP-treated dopaminergic neurons. We treated dopaminergic neuroblastoma SH-SY5Y cells with MPP^+. Immunoblotting revealed that treatment with MPP^+ generated a ~60-kDa protein band representing pATF6α (N) (Fig. 4, *A* and *B*) and induced phosphorylation of PERK (Fig. 4, *A* and *C*) as well as that of p38MAPK (Fig. 4, *A* and *D*) in SH-SY5Y cells as in the midbrain of ATF6α WT mice (see Fig. 2*A*). SB203585, an inhibitor of p38MAPK phosphorylation, attenuated p38MAPK phosphorylation induced by MPP^+ (Fig. 4, *A* and *D*) but showed little effect on the activation of ATF6α and PERK phosphorylation (Fig. 4, *A–C*). We confirmed that SB203585 attenuated p38MAPK phosphorylation without affecting cleavage of pATF6α (P) in MEFs treated with hydrogen peroxide (supplemental Fig. S2*A*). However, BiP was up-regulated after MPP^+ treatment and this up-regulation was significantly reduced by SB203585 in SH-SY5Y cells (Fig. 4, *A* and *E*). This observation was further confirmed by BiP promoter-luciferase reporter system (Fig. 4, *F* and *G*). The reporter gene −132/LUC contains a fragment of the BiP promoter driving the luciferase expression. We introduced the BiP promoter-luciferase plasmid into SH-SY5Y cells with or without p38MAPK overexpression vector, and then treated transfected cells with MPP^+. Luciferase expression level continuously increased for 24 h after MPP^+ treatment and this MPP^+-induced stimulation of reporter expression was synergistically enhanced by p38MAPK overexpression (Fig. 4*F*). We then examined the effect of MPP^+ and SB203585 on reporter expression in the primary co-culture of the midbrain and the striatum prepared from ATF6α KO or WT mice (supplemental Fig. 2*C*). We found that MPP^+ treatment induced a significant increment in luciferase expression in cells from ATF6α WT and that this effect was abrogated by the presence

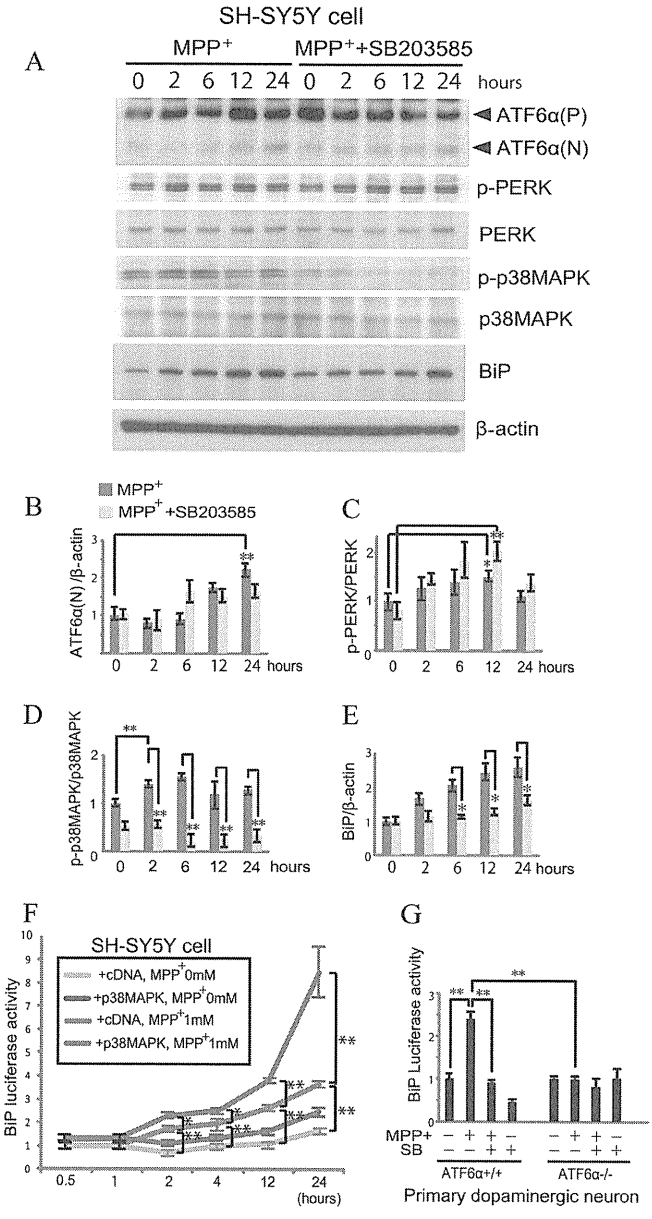

FIGURE 4. **Phosphorylated p38MAPK and activated ATF6α cooperate to enhance the expression level of BiP in dopaminergic neurons treated with MPP$^+$.** *A–E*, immunoblot of cell lysates from SH-SY5Y cells treated with 1 mM MPP$^+$ for 2, 6, 12, 24 h using anti-ATF6α, phosphorylated PERK (p-PERK), PERK, p38MAPK, phosphorylated p38MAPK (p-p38MAPK), BiP, and β-actin antibodies. 5 μM SB203585 was added into the medium prior to MPP$^+$ treatment for the indicated times. Densitometry of ATF6α (N) (*B*), p-PERK (*C*), p-p38MAPK (*D*), and BiP (*E*) was performed on scanned *immunoblots* images using the *Image-J and* normalized to β-actin, PERK, p38MAPK, and β-actin, respectively. Each bar denotes the mean ± S.D. *F*, BiP promoter-Luciferase plasmid and pRL-SV40 plasmid were transfected into SH-SY5Y cells with p38MAPK overexpression vector or Mock vector. Each group of transfected cells was treated with or without 1 mM MPP$^+$ for 0.5, 1, 2, 4, 12, 24 h. Relative activity is defined as the ratio of firefly luciferase activity to *Renilla* luciferase activity in dual-luciferase assay. *G*, dopaminergic neurons from primary co-culture of the midbrain and the striatum of ATF6α WT(+/+) or ATF6α KO(−/−) mice transfected with BiP promoter-Luciferase vector and pRL-SV40 vector and then treated with 1 mM MPP$^+$ for 24 h with or without 5 μM SB203585. Relative activity is defined as the ratio of firefly luciferase activity to *Renilla* luciferase activity in dual-luciferase assay.

of SB203585 (Fig. 4*G*). In contrast, reporter expression remained unchanged in MPP$^+$-treated cells derived from ATF6α KO. These data suggest that phosphorylation of p38MAPK induced by treatment with MPP$^+$ positively affects the ATF6α-mediated transcriptional induction of BiP.

MPP$^+$ Induces the Translocation of the N-terminal Fragment of ATF6α to the Nucleus and the Binding of N-terminal ATF6α with Phosphorylated p38MAPK and Enhances the Transcriptional Activity of ATF6α—To examine possible interaction between ATF6α and p38MAPK, we conducted immunofluorescence analysis of primary cultured dopaminergic neurons transfected with vectors to express green fluorescent protein (GFP) fused to the N terminus of full-length ATF6α (pGFP-ATF6α(P)), which is cleaved to produce nuclear-translocating pGFP-ATF6α(N) in response to ER stress (11), using anti-phosphorylated p38MAPK (p-p38MAPK) or anti-p38MAPK antibodies. GFP-ATF6α (P) was localized in the peri-nuclear region in non-stressed dopaminergic neurons (Fig. 5*A*) and was partially colocalized with cytosolic p38MAPK (Fig. 5*B*) in non-stressed dopaminergic neurons. 24 h after the treatment with MPP$^+$, pGFP-ATF6α (N) was translocated into the nucleus and colocalized with both DAPI and p-p38MAPK (Fig. 5*C*). By treating SH-SY5Y cells with MPP$^+$ after expression with both pGFP-ATF6α (P) and p38MAPK we confirmed that pGFP-ATF6α (N) was translocated into the nucleus and colocalized with both DAPI and p-p38MAPK (supplemental Fig. S3, *A–C*). To determine whether ATF6α physically associates with p-p38MAPK, we cotransfected flag-p38MAPK vector and the N-terminal fragment of ATF6α vector (1–373), abbreviated to N-ATF6α, into SH-SY5Y cells and performed immunoprecipitation with an anti-Flag antibody followed by immunoblotting with anti-ATF6α antibody. As shown in Fig. 5*D* (*upper panel*), pATF6α (N) (60kDa) and pATF6α (P) (90 kDa) were detected in the immunoprecipitates after treatment of MPP$^+$. SB203585 attenuated the intensity of both bands in immunoprecipitates from MPP$^+$-treated SH-SY5Y cells. Both pATF6α (N) (60 kDa) and pATF6α (P) (90 kDa) were also increased in the nuclear fraction of MPP$^+$-treated SH-SY5Y lysates after immunoprecipitation with anti-p-p38MAPK antibody as shown in Fig. 5*D* (*middle panel*). Endogenous N-ATF6α can bind to p-p38MAPK in MPP$^+$-treated condition and this binding was attenuated by adding SB203585 (Fig. 5*E*). Next we examined whether the p-p38MAPK-ATF6α complex binds to the promoter region of BiP in the nuclear fraction using ChIP assay. As shown in Fig. 5*F*, SH-SY5Y cells were treated with MPP$^+$ for 24 h and then cross-linked with formaldehyde. Extracted nuclear fraction was subjected to immunoprecipitation with p-p38MAPK antibody. Fragmented genomic DNA was extracted from the immunoprecipitates and quantified by QPCR using the primers for ERSEs of BiP promoter regions (−155~−21). MPP$^+$ enhanced the binding p-p38MAPK-ATF6α complex to ERSEs, which was reduced by p38MAPK inhibitor (Fig. 5, *G* and *H*). We amplified the other cis-elements on Neurogenin2 (a neural basic-loop-helix (bHLH) transcriptional factor, Ngn2) promoter using the genomic DNA extracted

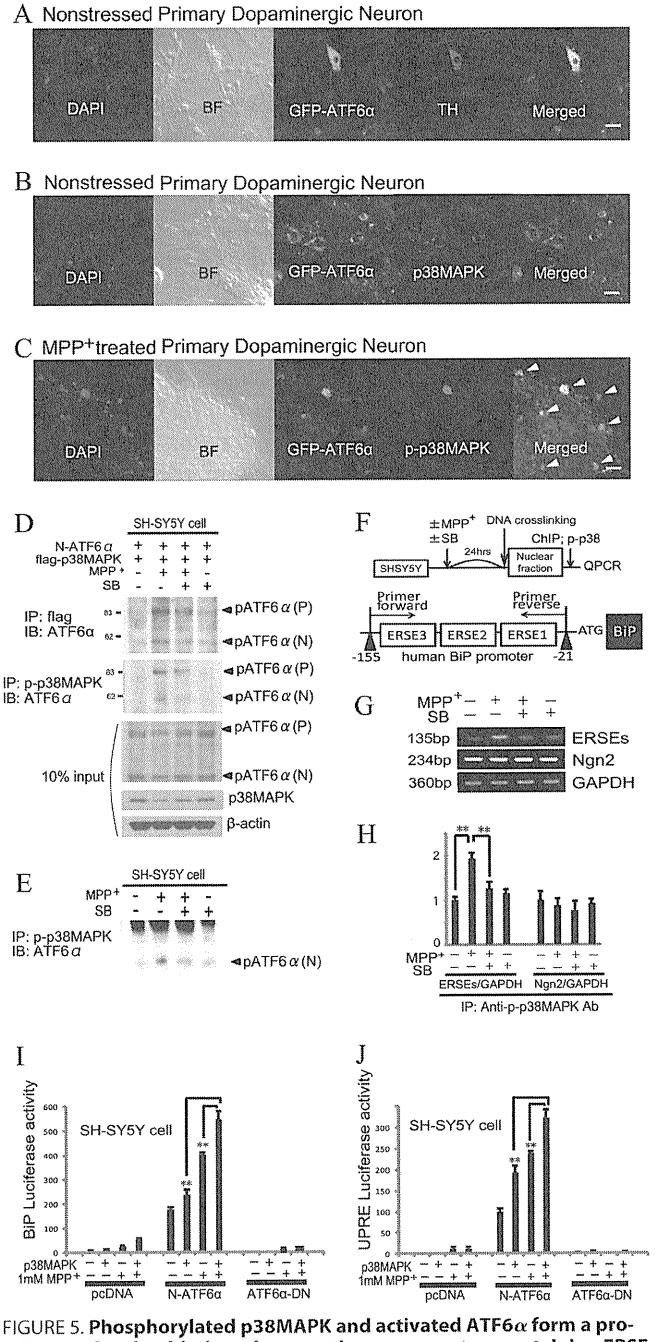

FIGURE 5. **Phosphorylated p38MAPK and activated ATF6α form a protein complex that binds and transactivates promoters containing ERSE and UPRE.** *A–C*, MPP^+ induces release of N-terminal ATF6α fragment with subsequent translocation into the nucleus and colocalization with phosphorylated p38MAPK in dopaminergic neurons. 24 h after transfection with pGFP-ATF6α (P), primary cultured dopaminergic neurons from co-culture of the midbrain and the striatum of ATF6α KO mice were fixed and stained with anti-TH antibody (*A*, *red*), anti-p38MAPK antibody (*B*, *red*), and DAPI (*blue*). 24 h after transfection with pGFP-ATF6α (P), primary cultured dopaminergic neurons were treated with 1 mM MPP^+ for 24 h, and then fixed for staining with phosphorylated p38MAPK (p-p38MAPK) antibody (*C*, *red*) and DAPI (*blue*). *White arrowheads* indicate the nuclear localization of DAPI, GFP, and p-p38MAPK. Scale bars indicate 10 μm. Abbreviations: *TH*, tyrosine hydroxylase; *BF*, bright-field image. *D–H*, MPP^+ treatment induces the binding among p-p38MAPK, N-terminal fragment of ATF6α and ERSEs of BiP promoter regions. SH-SY5Y cells were transfected with Flag-p38MAPK vector and N-terminal fragment of ATF6α-(1–373) vector. They were then cultured with or without 1 mM MPP^+ in the presence or absence of 5 μM SB203585 for 24 h. Cells were lysed in RIPA buffer and separated into soluble or insoluble fraction. *D*, soluble fraction was immunoprecipitated with anti-Flag antibody and immunoblotted with anti-ATF6α antibody (*upper panel*). Insoluble fraction was immunoprecipitated with anti-p-p38MAPK antibody and immunoblotted with anti-ATF6α antibody (*middle panel*). Western blot analysis of 10% input of soluble fraction was performed with anti-ATF6α, p38MAPK and β-actin antibodies (*lower panels*). Abbreviations: *IP*, immunoprecipitation; *IB*, immunoblotting; *SB*, SB203585; *N-ATF6α*, N-terminal fragment of ATF6α-(1–373). *E*, endogenous N-terminal fragment of ATF6α can bind to phosphorylated p38MAPK in MPP^+-treated condition. SHSY5Y cells were cultured without transfection and treated with or without 1 mM MPP^+ in the presence or absence of 5 μM SB203585 for 24 h. Cells were totally lysed in RIPA buffer using BIORUPTOR and immunoprecipitated with anti-p-p38MAPK antibody and immunoblotted with anti-ATF6α antibody. *F*, P-p38MAPK-ATF6α complex binds to ERSEs in response to MPP^+ treatment. *Upper panel* shows schematic representation of ChIP assays. SH-SY5Y cells were treated with or without MPP^+ in the presence or absence of 5 μM SB203585 for 24 h and then cross-linked with formaldehyde. Cells were lysed in RIPA buffer, and the insoluble fraction defined as nuclear fraction was lysed in SDS buffer. Immunoprecipitated with anti-p-p38MAPK, purified, and input DNAs were analyzed by Quantitative PCR using the primers shown in lower panel. *G*, primers used for human endogenous BiP promoter, Neurogenin2 (Ngn2) promoter and GAPDH yielded 135, 234, and 360 bp PCR products, respectively. *H*, values of PCR products were measured by QPCR and fold induction was defined as the value of BiP or Ngn2 promoter regions relative to the value of GAPDH. Each bar denotes the mean ± S.D. *I* and *J*, p38MAPK phosphorylation enhances the transcriptional activity of ATF6α. *I*, vectors(1 μg of BiP promoter-Luciferase vector, 100 ng of pRL-SV40 vector and 1 μg of control vector or p38MAPK vector) were mixed with 1 μg of Mock(pcDNA-3.1(+)) or N-terminal fragment (1–373)(N-ATF6α) or dominant-negative form (171–373) of ATF6α vector (ATF6α-DN) for transfection of SH-SY5Y cells in a 6-well dish for 48 h. Cells were challenged with or without 1 mM MPP^+ for 24 h and lysed for analysis of BiP reporter expression. *J*, vectors (1 μg 5 × UPRE reporter vector, 100 ng pRL-SV40 vector and 1 μg of control vector or p38MAPK vector) were mixed with 1 μg of pcDNA-3.1(+) or N-ATF6α or ATF6α-DN vector for transfection of SH-SY5Y cells in a 6-well dish for 48 h. Cells were challenged with or without 1 mM MPP^+ for 24 h and lysed for analysis of UPRE reporter expression.

from the same immunoprecipitated samples and found that the amplified PCR products of the Ngn2 promoter regions were not increased in MPP^+-treated SH-SY5Y cells. Thus, phosphorylated p38MAPK selectively binds to the activated and cleaved N-terminal fragment of ATF6α that binds to the ERSEs on BiP promoter region in MPP^+-treated cells.

We finally investigated whether the expression of p38MAPK and/or the treatment with MPP^+ could increase the transcriptional activity of nuclear-translocating ATF6α using the BiP promoter-luciferase system. MPP^+ was added to SH-SY5Y cells cotransfected with Mock or N-ATF6α encoding transactivator domain (TAD) and the DNA-binding b-ZiP domain or the dominant-negative form lacking TAD of ATF6α (ATF6α-DN) in the presence or absence of p38MAPK. MPP^+ treatment significantly enhanced the stimulative effect of p38MAPK on N-ATF6α-mediated activation of BiP reporter expression (Fig. 5*I*). We also found that MPP^+ treatment increased transcriptional activator activity of N-ATF6α through UPRE, which has been shown to be present in the promoter region of ERAD components and be functional in the induction of ERAD components (22, 23), and further enhanced it in presence of p38MAPK (Fig. 5*J*). ATF6α-DN canceled these enhancement induced by p38MAPK overexpression through ERSE and UPRE. Thus, MPP^+ promotes phosphorylation of p38MAPK and the binding with the N-terminal ATF6α, leading to up-regulation of ATF6α transcriptional activity.

Hydrogen peroxide also induced the translocation of the N-terminal fragment of ATF6α into the nucleus, where it co-localizes with p-p38MAPK (supplemental Fig. S3, *D–G*). Hydrogen peroxide promoted the binding of N-ATF6α with phosphorylated p38MAPK and enhanced the transcriptional activity of N-ATF6α through ERSE and UPRE (supplemental Fig. S3, *H–J*).

DISCUSSION

In this study, we concluded that ATF6α plays an important role in protection from MPTP toxicity in the dopaminergic neurons via up-regulation of ER chaperones and ERAD component. This was based on the following findings: 1) ATF6α controls the levels of ER chaperones and ERAD component in dopaminergic neurons-containing brain regions (Figs. 1, *A–D*) and 2). Both MPTP and MPP^+ upregulate the expression levels of ER chaperones and ERAD component by activating ATF6α in dopaminergic neurons and SH-SY5Y cells (Fig. 2, *A, B, C, F, G, H* and 4, *A, B, E, F,* and *G*); 3) MPTP triggers more formation of clusters of ubiquitin-immunoreactive material in the striatum of ATF6α KO mice than in WT mice (Fig. 3, *A* and *B*); 4) Dopaminergic neurons under ATF6α KO conditions are more vulnerable to MPTP neurotoxicity (Fig. 3, *C–F*). Previous studies showed that MPTP and 6-OHDA induce various ER stress mediators *in vitro* (24–26). However, it has been unclear how these neurotoxins induce UPR.

A plausible mechanism is that MPTP decreases the protein degradation function of striatal UPS (27). A single or intermittent dose of MPTP decreases UPS activity only for a short time and does not lead to the ubiquitinated inclusion bodies in rodent brain (28). In contrast, continuous MPTP administration causes long-lasting impairment of UPS and the production of inclusion bodies immunoreactive for ubiquitin and α-synuclein in the rodent SNc (27). This report suggests that the inhibition of UPS by MPTP causes the accumulation of unfolded proteins followed by activation of UPR, finally leading to ER stress-induced cell death.

Consistent with this hypothesis, our study demonstrated that UPR attenuation caused by ATF6α deletion accelerates the MPTP-induced formation of ubiquitin immunopositive inclusion body in the striatum as well as dopaminergic neuronal death (Fig. 3). This result suggests that MPTP induces accumulation of ubiquitin-positive aggregates presumably as a result of oxidative protein damage to protein folding and its machineries (29–31) and that activated ATF6α promotes refolding and/or elimination of ubiquitinated proteins in the nerve terminal of dopaminergic neuron by the action of induced ER chaperones and ERAD components. These findings strongly suggest that both UPS and UPR are involved in MPTP-induced dopaminergic neuronal depletion. In our study we stained the striatal sections from MPTP-treated ATF6α WT and KO mice with thioflavin T (amyloid-specific dye) and immunostained with anti-α-synuclein antibody and anti-phosphorylated α-synuclein. However we could not detect any stained aggregates for them (supplemental Fig. S2*B*). Although it remains to be elucidated what is the major component of the ubiquitinated aggregates in this study, we speculates that oxidative products should be ubiquitinated and accumulated after oxidative stress induced by MPTP.

MPP^+ interferes with the mitochondrial complex-1, generates ROS. ROS are also generated in the degradation process of dopamine and therefore dopamine is the most oxidative neurotransmitter in brain (16). In the present study, ATF6α was activated particularly in the dopaminergic neuron system (Fig. 1, *A* and *B*) and the metabolism of dopamine is decreased in ATF6α KO mice (Fig. 1*E*), suggesting that ROS generated from dopamine metabolic process may play a critical role in the up-regulation of ATF6α-mediated UPR.

Previous study showed that ROS induced by both MPP^+ and dopamine metabolism promotes phosphorylation of p38MAPK (17, 18, 32). Phosphorylated p38MAPK phosphorylates ATF6α and mediates the transcriptional induction of the atrial natriuretic factor gene through a serum response element (21, 33). To explore the relationship between oxidative stress by ROS and UPR by ATF6α, we focused on p38MAPK.

We demonstrated that: 1) Both MPTP and MPP^+ induce the phosphorylation of p38MAPK in dopaminergic neurons as well as in SH-SY5Y cells (Figs. 2, *A, E, K, L* and 4, *A* and *D*). 2) MPP^+ induces ATF6α-mediated up-regulation of BiP expression level in a p38MAPK-dependent manner (Fig. 4, *A, E, F,* and *G*). 3) MPP^+ triggers the translocation of N-terminal ATF6α to the nucleus and the binding of N-terminal ATF6α with phosphorylated p38MAPK to enhance the transcriptional activity of ATF6α in dopaminergic neurons (Fig. 5, *C–J*). Hydrogen peroxide, a representative ROS, also activated ATF6α and phosphorylated p38MAPK (supplemental Fig. S2*A*). Hydrogen peroxide promoted the formation of N-ATF6α-p-p38MAPK complex and enhanced the transcriptional activity of ATF6α to up-regulate ER chaperones and ERAD components (supplemental Fig. S3, *D–J*).

Based on these data, we propose that MPP^+-derived oxidative stress results in phosphorylation of p38MAPK, enhancement of ATF6α transcriptional activity, induction of ER chaperones and ERAD components and degradation of ubiquitinated accumulated proteins in dopaminergic neurons. In contrast, under ATF6α-deleted condition, MPP^+ triggers the formation of ubiquitinated aggregates in the striatum, and this protein accumulation lead to apoptosis of the dopaminergic neurons (Fig. 6).

ER stress and oxidative stress are closely linked events. Another oxidative neurotoxin, 6-OHDA, causes rapid generation of ROS, oxidative modification of protein and activates UPR. Antioxidants reduce UPR activation and apoptosis, and improve protein secretion (29). This study suggests that UPR protects against oxidative stress-induced cell death. ER stress preconditioning of BiP attenuates H_2O_2-induced cell injury in LLC-PK1 cells (34). Precondition of ER chaperones in the striatum expressed by ATF6α under physiological conditions may also suppress dopaminergic neurons depletion induced by MPP+-derived oxidative stress.

The p38MAPK pathway is stimulated by cellular stresses, such as free radicals and inflammatory agents, and mediates

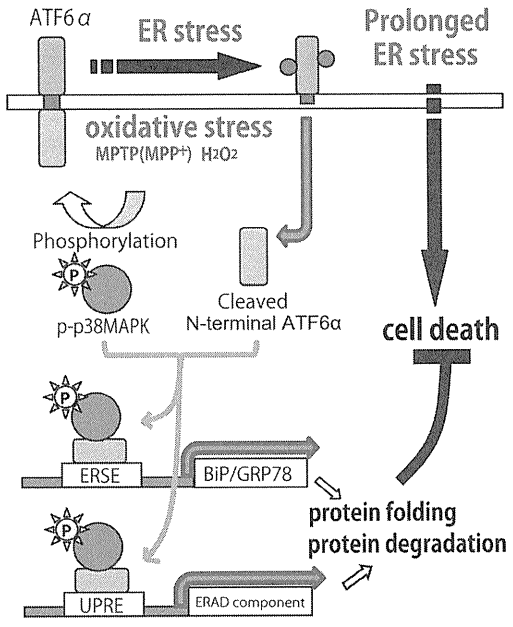

FIGURE 6. **A proposed model for oxidative stress-ER stress pathway mediated by p38MAPK-ATF6α interaction.** Oxidative stress induced by MPTP (MPP^+) or hydrogen peroxide (H_2O_2) cleaves proteolytic N-terminal fragment of ATF6α and up-regulates the phosphorylation of p38MAPK. Phosphorylated p38MAPK binds to N-terminal fragment of ATF6α and enhances ATF6α-mediated induction of ER chaperones and ERAD components. This results in the degradation of accumulated unfolded proteins and prevents ER stress-induced dopaminergic neuronal death.

various kinds of signaling cascades, including; the cell cycle, apoptosis, and cell survival. Previous studies reported that p38MAPK plays a critical role in suppressing ER stress-induced macrophage apoptosis *in vitro* and advanced lesional macrophage apoptosis *in vivo* (35). On the contrary, p38MAPK also has a pro-apoptotic role in maintaining homeostasis under various stresses. Phosphorylation of p53 following phosphorylation of p38MAPK up-regulates transcription of Bax and Puma, leading to apoptotic cell death (18). Whether p38MAPK serves as pro- or anti-apoptotic agent seems to be context-dependent.

It should be noted that p38MAPK does not activate ATF6α (Fig. 5*I*) and a p38MAPK phosphorylation inhibitor does not suppress proteolytic cleavage of N-terminal ATF6α in our *vitro* study (Fig. 4*B* and supplemental Fig. S2*A*). This suggests that neither p38MAPK nor phospho-p38MAPK initiates ATF6α-mediated UPR. Mechanism underlying oxidative stress-mediated ATF6α cleavage should be elucidated in the future.

The interaction between phosphorylated p38MAPK and cleaved N-terminal ATF6α could results in a protective effect against the vicious cycle of oxidative stress-ER stress by induction of ER chaperones and ERAD components. This p38MAPK-ATF6α interaction provides a new link between oxidative stress and ER stress. ATF6α-mediated induction of ER chaperones and ERAD components via p38MAPK pathway may provide a therapeutic target for Parkinson disease and other neurodegenerative diseases associated with protein misfolding.

REFERENCES

1. Valente, E. M., Abou-Sleiman, P. M., Caputo, V., Muqit, M. M., Harvey, K., Gispert, S., Ali, Z., Del Turco, D., Bentivoglio, A. R., Healy, D. G., Albanese, A., Nussbaum, R., González-Maldonado, R., Deller, T., Salvi, S., Cortelli, P., Gilks, W. P., Latchman, D. S., Harvey, R. J., Dallapiccola, B., Auburger, G., and Wood, N. W. (2004) *Science* **304,** 1158–1160
2. Imai, Y., Soda, M., Inoue, H., Hattori, N., Mizuno, Y., and Takahashi, R. (2001) *Cell* **105,** 891–902
3. Uehara, T., Nakamura, T., Yao, D., Shi, Z. Q., Gu, Z., Ma, Y., Masliah, E., Nomura, Y., and Lipton, S. A. (2006) *Nature* **441,** 513–517
4. Wang, H. Q., Imai, Y., Inoue, H., Kataoka, A., Iita, S., Nukina, N., and Takahashi, R. (2008) *J. Neurochem.* **107,** 171–185
5. Trojanowski, J. Q., and Lee, V. M. (1998) *Arch. Neurol.* **55,** 151–152
6. Mori, K. (2000) *Cell* **101,** 451–454
7. Yamamoto, K., Sato, T., Matsui, T., Sato, M., Okada, T., Yoshida, H., Harada, A., and Mori, K. (2007) *Dev. Cell* **13,** 365–376
8. Wu, J., Rutkowski, D. T., Dubois, M., Swathirajan, J., Saunders, T., Wang, J., Song, B., Yau, G. D., and Kaufman, R. J. (2007) *Dev. Cell* **13,** 351–364
9. Rutkowski, D. T., Wu, J., Back, S. H., Callaghan, M. U., Ferris, S. P., Iqbal, J., Clark, R., Miao, H., Hassler, J. R., Fornek, J., Katze, M. G., Hussain, M. M., Song, B., Swathirajan, J., Wang, J., Yau, G. D., and Kaufman, R. J. (2008) *Dev. Cell* **15,** 829–840
10. Haze, K., Okada, T., Yoshida, H., Yanagi, H., Yura, T., Negishi, M., and Mori, K. (2001) *Biochem. J.* **355,** 19–28
11. Nadanaka, S., Yoshida, H., Kano, F., Murata, M., and Mori, K. (2004) *Mol. Biol. Cell* **15,** 2537–2548
12. Adachi, Y., Yamamoto, K., Okada, T., Yoshida, H., Harada, A., and Mori, K. (2008) *Cell Struct. Funct.* **33,** 75–89
13. Yoshida, H., Haze, K., Yanagi, H., Yura, T., and Mori, K. (1998) *J. Biol. Chem.* **273,** 33741–33749
14. Haze, K., Yoshida, H., Yanagi, H., Yura, T., and Mori, K. (1999) *Mol. Biol. Cell* **10,** 3787–3799
15. Yokoyama, H., Kuroiwa, H., Yano, R., and Araki, T. (2008) *Neurol. Sci.* **29,** 293–301
16. Eisenhofer, G., Kopin, I. J., and Goldstein, D. S. (2004) *Pharmacol. Rev.* **56,** 331–349
17. Junn, E., and Mouradian, M. M. (2001) *J. Neurochem.* **78,** 374–383
18. Karunakaran, S., Saeed, U., Mishra, M., Valli, R. K., Joshi, S. D., Meka, D. P., Seth, P., and Ravindranath, V. (2008) *J. Neurosci.* **28,** 12500–12509
19. Gomez-Lazaro, M., Galindo, M. F., Concannon, C. G., Segura, M. F., Fernandez-Gomez, F. J., Llecha, N., Comella, J. X., Prehn, J. H., and Jordan, J. (2008) *J. Neurochem.* **104,** 1599–1612
20. Newhouse, K., Hsuan, S. L., Chang, S. H., Cai, B., Wang, Y., and Xia, Z. (2004) *Toxicol. Sci.* **79,** 137–146
21. Thuerauf, D. J., Arnold, N. D., Zechner, D., Hanford, D. S., DeMartin, K. M., McDonough, P. M., Prywes, R., and Glembotski, C. C. (1998) *J. Biol. Chem.* **273,** 20636–20643
22. Yamamoto, K., Yoshida, H., Kokame, K., Kaufman, R. J., and Mori, K. (2004) *J. Biochem.* **136,** 343–350
23. Yamamoto, K., Suzuki, N., Wada, T., Okada, T., Yoshida, H., Kaufman, R. J., and Mori, K. (2008) *J. Biochem.* **144,** 477–486
24. Holtz, W. A., and O'Malley, K. L. (2003) *J. Biol. Chem.* **278,** 19367–19377
25. Ryu, E. J., Harding, H. P., Angelastro, J. M., Vitolo, O. V., Ron, D., and Greene, L. A. (2002) *J. Neurosci.* **22,** 10690–10698
26. Silva, R. M., Ries, V., Oo, T. F., Yarygina, O., Jackson-Lewis, V., Ryu, E. J., Lu, P. D., Marciniak, S. J., Ron, D., Przedborski, S., Kholodilov, N., Greene, L. A., and Burke, R. E. (2005) *J. Neurochem.* **95,** 974–986
27. Fornai, F., Schlüter, O. M., Lenzi, P., Gesi, M., Ruffoli, R., Ferrucci, M., Lazzeri, G., Busceti, C. L., Pontarelli, F., Battaglia, G., Pellegrini, A., Nicoletti, F., Ruggieri, S., Paparelli, A., and Südhof, T. C. (2005) *Proc. Natl. Acad. Sci. U.S.A.* **102,** 3413–3418
28. Shimoji, M., Zhang, L., Mandir, A. S., Dawson, V. L., and Dawson, T. M. (2005) *Brain Res. Mol. Brain Res.* **134,** 103–108
29. Holtz, W. A., Turetzky, J. M., Jong, Y. J., and O'Malley, K. L. (2006)

J. Neurochem. **99,** 54–69
30. Haynes, C. M., Titus, E. A., and Cooper, A. A. (2004) *Mol. Cell* **15,** 767–776
31. Malhotra, J. D., Miao, H., Zhang, K., Wolfson, A., Pennathur, S., Pipe, S. W., and Kaufman, R. J. (2008) *Proc. Natl. Acad. Sci. U.S.A.* **105,** 18525–18530
32. Du, Y., Ma, Z., Lin, S., Dodel, R. C., Gao, F., Bales, K. R., Triarhou, L. C., Chernet, E., Perry, K. W., Nelson, D. L., Luecke, S., Phebus, L. A., Bymaster, F. P., and Paul, S. M. (2001) *Proc. Natl. Acad. Sci. U.S.A.* **98,** 14669–14674
33. Luo, S., and Lee, A. S. (2002) *Biochem. J.* **366,** 787–795
34. Hung, C. C., Ichimura, T., Stevens, J. L., and Bonventre, J. V. (2003) *J. Biol. Chem.* **278,** 29317–29326
35. Seimon, T. A., Wang, Y., Han, S., Senokuchi, T., Schrijvers, D. M., Kuriakose, G., Tall, A. R., and Tabas, I. A. (2009) *J. Clin. Invest.* **119,** 886–898

Neurobiology of Disease

Induced Loss of ADAR2 Engenders Slow Death of Motor Neurons from Q/R Site-Unedited GluR2

Takuto Hideyama,[1,2] Takenari Yamashita,[1,2] Takeshi Suzuki,[3] Shoji Tsuji,[2] Miyoko Higuchi,[5] Peter H. Seeburg,[5] Ryosuke Takahashi,[6] Hidemi Misawa,[4] and Shin Kwak[1,2]

[1]Core Research for Evolutional Science and Technology, Japan Science and Technology Agency and [2]Department of Neurology, Graduate School of Medicine, University of Tokyo, Bunkyo-ku, Tokyo 113-8655, Japan, [3]Division of Basic Biological Sciences and [4]Department of Pharmacology, Faculty of Pharmacy, Keio University, Minato-ku, Tokyo 105-8512, Japan, [5]Department of Molecular Neuroscience, Max Planck Institute of Medical Research, 69120 Heidelberg, Germany, and [6]Department of Neurology, Graduate School of Medicine, University of Kyoto, Sakyo-ku, Kyoto 606-8507, Japan

GluR2 is a subunit of the AMPA receptor, and the adenosine for the Q/R site of its pre-mRNA is converted to inosine (A-to-I conversion) by the enzyme called adenosine deaminase acting on RNA 2 (ADAR2). Failure of A-to-I conversion at this site affects multiple AMPA receptor properties, including the Ca^{2+} permeability of the receptor-coupled ion channel, thereby inducing fatal epilepsy in mice (Brusa et al., 1995; Feldmeyer et al., 1999). In addition, inefficient GluR2 Q/R site editing is a disease-specific molecular dysfunction found in the motor neurons of sporadic amyotrophic lateral sclerosis (ALS) patients (Kawahara et al., 2004). Here, we generated genetically modified mice (designated as AR2) in which the ADAR2 gene was conditionally targeted in motor neurons using the Cre/loxP system. These AR2 mice showed a decline in motor function commensurate with the slow death of ADAR2-deficient motor neurons in the spinal cord and cranial motor nerve nuclei. Notably, neurons in nuclei of oculomotor nerves, which often escape degeneration in ALS, were not decreased in number despite a significant decrease in GluR2 Q/R site editing. All cellular and phenotypic changes in AR2 mice were prevented when the mice carried endogenous GluR2 alleles engineered to express edited GluR2 without ADAR2 activity (Higuchi et al., 2000). Thus, loss of ADAR2 activity causes AMPA receptor-mediated death of motor neurons.

Introduction

GluR2 (also known as GluR-B or GluA2) is a subunit of the AMPA receptor. The adenosine within the glutamine codon for the Q/R site of its pre-mRNA is converted to inosine (A-to-I conversion) (Yang et al., 1995) by adenosine deaminase acting on RNA 2 (ADAR2) (Melcher et al., 1996). Because inosine is read as guanosine during translation, the genomic glutamine codon (Q: CAG) is converted to a codon for arginine (R: CIG) at the Q/R site of GluR2 in virtually all neurons in the mammalian brain (Seeburg, 2002). Conversion of Q to R at the Q/R site of GluR2 affects multiple AMPA receptor properties, including the Ca^{2+} permeability of the receptor-coupled ion channel, receptor trafficking, and assembly of receptor subunits (Sommer et al., 1991; Burnashev et al., 1992; Greger et al., 2002, 2003). Genetically modified mice in which the Q/R site of GluR2 remains unedited displayed fatal status epilepticus at early postnatal stages with exaggerated excitation of neurons (Brusa et al., 1995; Feldmeyer et al., 1999). Systemic ADAR2-null mice exhibit a similar phenotype, which was attributed to the absence of GluR2 Q/R site RNA editing (Higuchi et al., 2000). These findings indicate that the A-to-I conversion of the GluR2 Q/R site by ADAR2 is crucial for survival in mice. However, it has not been demonstrated whether neuronal death occurs in mice lacking GluR2 Q/R site editing or in those lacking ADAR2.

Amyotrophic lateral sclerosis (ALS) is the most common adult-onset motor neuron disease. Patients with sporadic ALS account for >90% of all cases, and the majority of them do not carry mutations in the causative genes of familial ALS that have been identified thus far (Schymick et al., 2007; Beleza-Meireles and Al-Chalabi, 2009). There is strong evidence indicating that AMPA receptor-mediated excitotoxic mechanism plays a pathogenic role in ALS and SOD1-associated familial ALS model animals (Rothstein et al., 1992; Carriedo et al., 1996; Van Damme et al., 2005). Recently, we demonstrated that a significant proportion of GluR2 mRNA was unedited at the Q/R site in spinal motor neurons of postmortem patients with sporadic ALS. This is in marked contrast to the fact that all GluR2 mRNA was edited in the motor neurons of control subjects (Takuma et al., 1999; Kawahara et al., 2004) and of patients with motor neuron diseases other than sporadic ALS (Kawahara et al., 2006), as well as in dying neurons in other neurodegenerative diseases, including Purkinje cells of patients with spinocerebellar degeneration (Paschen et al., 1994; Akbarian et al., 1995; Kawahara et al., 2004; Suzuki et al., 2003). The disease specificity of inefficient GluR2 Q/R site editing implies the pathogenic relevance of ADAR2 insufficiency in the death of motor neurons in sporadic ALS but

Received April 20, 2010; revised July 2, 2010; accepted July 13, 2010.

This study was supported in part by Ministry of Education, Culture, Sports, Science, and Technology of Japan Grants-in-Aid for Scientific Research 17390251, 19390235, and 20023008 (S.K.), Ministry of Health, Labor, and Welfare of Japan Grant H18-Kokoro-017 (S.K.), and Amyotrophic Lateral Sclerosis Association Grant 875 (P.H.S.). We thank Dr. R. B. Emeson at Vanderbilt University (Nashville, TN) for antibodies to ADAR2 and D. Kimura, K. Awabayashi, Dr. J. Shimizu, Dr. M. Fukaya, and T. Kakinoki for technical assistance.

Correspondence should be addressed to Dr. Shin Kwak, Department of Neurology, Graduate School of Medicine, University of Tokyo, 7-3-1 Hongo, Bunkyo-ku, Tokyo 113-8655, Japan. E-mail: kwak-tky@umin.ac.jp.

DOI:10.1523/JNEUROSCI.2021-10.2010

 0270-6474/10/3011917-09$15.00/0

leaves open the possibility that other genes whose products remain unedited by ADAR2 insufficiency might contribute to the demise of motor neurons.

We therefore generated a conditional ADAR2 knock-out mouse strain (designated here as AR2), using the Cre/loxP recombination system, and demonstrated that the loss of ADAR2 activity induces the slow death of motor neurons also in the mouse. Importantly, all motor neuron death in AR2 mice could be prevented by substituting the wild-type GluR2 alleles for alleles point mutated to express Q/R site-edited GluR2 in the absence of ADAR2. Our genetic studies in the mouse clearly demonstrate that the underediting of the GluR2 Q/R site specifically induces death of motor neurons with reduced ADAR2 activity.

Materials and Methods

All studies were performed in accordance with the Declaration of Helsinki, the Guideline of Animal Studies of the University of Tokyo, and National Institutes of Health. The committee of animal handling of the University of Tokyo also approved the experimental procedures used.

ADAR2^{flox} allele and conditional ADAR2 knock-out mice. DNA for the targeted region was obtained from a mouse strain 129/SvEv genomic library (supplemental Table S1, available at www.jneurosci.org as supplemental material). A LoxP site was inserted into intron 6 and another LoxP site was inserted into intron 9 of the mouse *ADAR2* gene (*adarb1*), along with a selection cassette containing a neomycin resistance gene (Neo) flanked by flippase recognition target (FRT) sites (Fig. 1*A*). Exons 7–9 encode the majority of the adenosine deaminase motif. Chimeric mice were generated by injection of a targeted embryonic stem cell clone into C57BL/6-derived blastocysts. *ADAR2$^{flox/+}$* intercrosses produced *ADAR2$^{flox/flox}$* mice at apparent Mendelian frequencies, and *ADAR2$^{flox/flox}$* homozygous mice were phenotypically normal. Determination of the *ADAR2^{flox}* allele was conducted by genomic PCR (Fig. 1*B*). Then, to knock-out ADAR2 activity selectively in motor neurons, we crossed *ADAR2$^{flox/flox}$* mice with VAChT–Cre.Fast mice to obtain AR2 mice.

AR2 mice. Intercrosses of *ADAR2$^{flox/+}$*/VAChT–Cre.Fast mice produced *ADAR2$^{flox/flox}$*/VAChT–Cre.Fast (AR2) mice, either heterozygous or homozygous for the Cre transgene, which directs restricted Cre expression under the control of the vesicular acetylcholine transporter gene promoter in a subset of cholinergic neurons, including the spinal motor neurons (Misawa et al., 2003). Cre expression levels were found not to differ in mice heterozygous or homozygous for the VAChT–Cre.Fast transgene (Misawa et al., 2003). The same intercrosses also produced, as littermates of AR2, *ADAR2$^{flox/flox}$* (Ctl1) and *ADAR2$^{+/+}$*/VAChT–Cre-.Fast mice (Ctl2), which were used as controls. Both genders of AR2 and control mice were used, but littermates heterozygous for the floxed ADAR2 allele were not used in this study. All genotyping was performed by PCR on DNA from tail biopsies. PCR primers and amplicon sizes for the different alleles are listed in supplemental Table S1 (available at www.jneurosci.org as supplemental material).

AR2/GluR-B$^{R/R}$ mice. AR2/GluR-*B$^{R/R}$* mice were generated by intercrossing ADAR2$^{flox/+}$/VAChT–Cre.Fast/GluR-*B$^{R/+}$* mice, which had been produced by crossbreeding AR2 mice with GluR-*B$^{R/R}$* mice. The AR2/GluR-*B$^{R/R}$* mice used by us were either heterozygous or homozygous for the Cre transgene (Misawa et al., 2003) and homozygous for the floxed ADAR2 and the GluR-B(R) allele. The desired genotype was found approximately once in every 20 offspring. Other genotypes produced by the intercrosses were not used in this study. All genotyping for the ADAR2 and GluR2 (GluR-B) alleles as well as for the Cre transgene was by PCR on DNA extracted from tail biopsies. PCR primers and amplicon sizes for the different alleles are listed in supplemental Table S1 (available at www.jneurosci.org as supplemental material).

Genomic PCR and reverse transcription-PCR. Genomic DNA was extracted from mouse tails using the High Pure PCR Template Preparation kit (Roche). Total RNA was isolated from brain and spinal cord tissue, and first-strand cDNA was synthesized and then treated with DNase I (Invitrogen) as described previously (Kawahara et al., 2003b). Primer pairs and the conditions used for PCR are presented in supplemental Table S1 (available at www.jneurosci.org as supplemental material). Positions of primer pairs used for genomic ADAR2 PCR (Fig. 1*A*, F1/R1) and ADAR2 reverse transcription (RT)-PCR (Fig. 1*C*, F2/R2) are indicated.

Analysis for editing efficiency at A-to-I sites. Editing efficiencies at the Q/R sites in GluR2 mRNAs were calculated by quantitative analyses of the digests of RT-PCR products with BbvI as described previously (Takuma et al., 1999; Kawahara et al., 2003a, 2004). In brief, 2 μl of cDNA were subjected to first PCR in duplicate in a reaction mixture of 50 μl containing 200 mM each primer, 1 mM dNTP Mix (Eppendorf), 5 μl of 10× PCR buffer, and 1 μl of Advantage 2 Polymerase mix (Clontech). The PCR amplification began with a 1 min denaturation step at 95°C, followed by 40 cycles of denaturation at 95°C for 10 s, annealing at 60°C for 30 s, and extension at 68°C for 40 s. Nested PCR was conducted on 2 μl of the first PCR product under the same conditions with the exception of the annealing temperature (58°C). Primer pairs used for each PCR were listed in supplemental Table S1 (available at www.jneurosci.org as supplemental material). After gel purification using the Zymoclean Gel DNA Recovery kit according to the protocol of the manufacturer (Zymo Research), an aliquot (0.5 mg) was incubated with BbvI (New England Biolabs) at 37°C for 12 h. The PCR products originating from Q/R site-edited GluR2 mRNA had one intrinsic restriction enzyme recognition site, whereas those originating from unedited mRNA had an additional recognition site. Thus, restriction digestion of the PCR products originating from edited GluR2 mRNA should produce different numbers of fragments (two bands at 219 and 59 bp) from those originating from unedited GluR2 mRNA (three bands at 140, 79, and 59 bp). Because the 59 bp band would originate from both edited and unedited mRNA but the 219 bp band would originate from only edited mRNA, we quantified the molarity of the 219 and 59 bp bands using the 2100 Bioanalyzer (Agilent Technologies) and calculated the editing efficiency as the ratio of the former to the latter for each sample (supplemental Table S1, available at www.jneurosci.org as supplemental material).

With similar methods, we calculated the editing efficiencies at the Q/R sites in GluR5 and GluR6 mRNA and in GluR2 pre-mRNA, the R/G site in GluR2 mRNA, and the I/V site in Kv1.1 mRNA (Paschen et al., 1994; Takuma et al., 1999; Kawahara et al., 2003a, 2004; Nishimoto et al., 2008). The following restriction enzymes were used for restriction digestion of the respective A-to-I sites: BbvI for the Q/R sites, MfeI (New England Biolabs) for the I/V site, and MseI (New England Biolabs) for the R/G site. Primer pairs used for each PCR and sizes of restriction digests of PCR products were indicated in supplemental Table S1 (available at www.jneurosci.org as supplemental material).

Behavioral analyses. Using a mouse-specific rotarod (SN-445; Neuroscience Corp.), we determined the maximal time before falling at 10 rpm during a 180 s period; each run consisted of three trials. Grip strength was measured with a dynamometer (NS-TRM-M; Neuroscience Corp.). Measurements were conducted weekly by a researcher blind to genotype and age of the mice.

Isolation of single motor neurons and brain tissue. Single-cell isolation from frozen spinal cord tissue was performed with a laser microdissection system (Leica AS LMD; Leica Microsystems) as described previously (Kawahara et al., 2003b, 2004). All of the large motor neurons (diameter larger than 20 μm) in the anterior horn were dissected from 14-μm-thick cervical cord sections, and three neurons each were collected together into respective single test tubes containing 200 μl of TRIZOL Reagent. In addition, using the same method, nuclei of oculomotor nerve and of facial nerve were dissected from the brainstem sections of AR2 mice and control mice at 12 months of age. The positions of these cranial nerve nuclei were identified using the Paxinos and Franklin mouse brain atlas (Paxinos and Franklin, 2001). All samples were kept at −20°C until use.

Immunohistochemistry. Under deep anesthesia with isoflurane, mice were transcardially perfused with 3% paraformaldehyde and 1% glutaraldehyde in PBS. The brains and spinal cords were removed and immersed in serially increasing concentrations of a sucrose–PBS solution (final sucrose concentration of 30%). The immunohistochemical procedure was performed on 10-μm-thick sections, which were cut with a cryostat (model HM500 O; Microm). The sections were analyzed with a

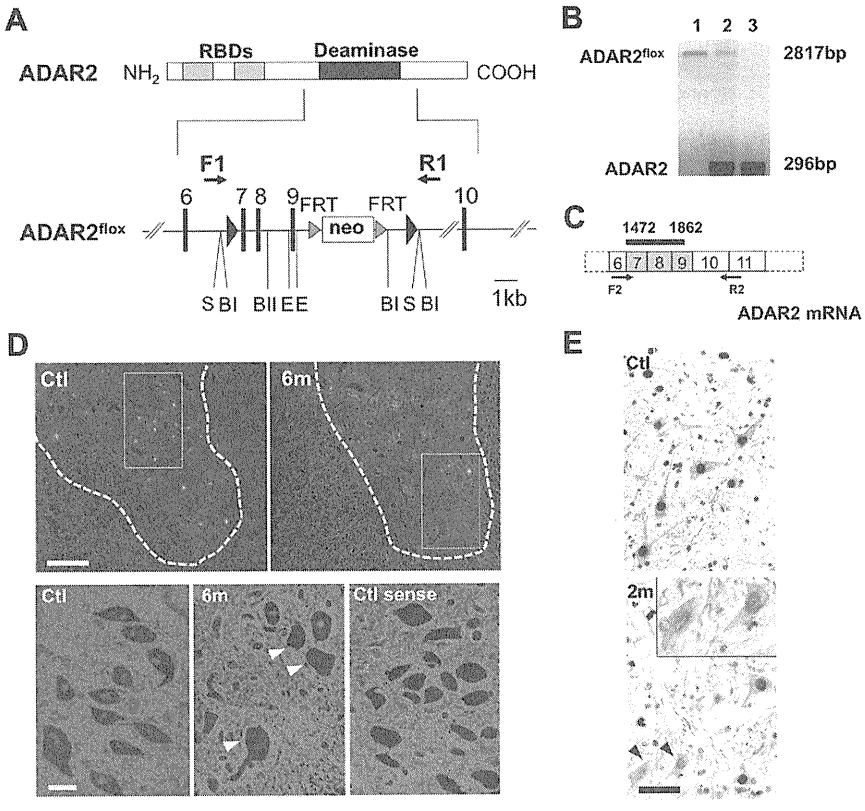

Figure 1. Generation of a conditional ADAR2 knock-out mouse. ***A***, A LoxP site (filled triangle) was inserted into intron 6 and another LoxP site in intron 9 with a selection cassette containing the gene for neomycin resistance (Neo) flanked by FRT sites. Exons are depicted as black bars with numbers. RBDs, RNA binding domains; F1/R1, primer pair (supplemental Table S1, available at www.jneurosci.org as supplemental material) for ***B***; S, SfiI; BI, BglI; BII, BglII; E, ERI. ***B***, Genomic PCR using template DNA obtained from the tails of *ADAR2*$^{flox/flox}$ mice (lane 1), *ADAR2*$^{flox/+}$ mice (lane 2), and *ADAR2*$^{+/+}$ mice (lane 3). ***C***, Exons excised by recombination are shown as shaded areas in the mRNA, and a black bar indicates the *in situ* hybridization probe (supplemental Table S1, available at www.jneurosci.org as supplemental material) for ***D***. F2/R2, Primer pair (supplemental Table S1, available at www.jneurosci.org as supplemental material) used in Figure 2*B*. ***D***, *In situ* hybridization using a probe that encompasses the region excised by Cre-mediated recombination. There is a large number of punctate signals in the gray matter (outlined with dotted lines) of control mice (Ctl), whereas nuclei of some large neurons in the anterior horn were devoid of signal in the *ADAR2*$^{flox/flox}$/VAChT–Cre.Fast (AR2) mice at 6 months of age (6m; arrowheads in magnified view). The sense probe did not yield a visible signal in the control mice at the same age (Ctl sense). Scale bars: top panels, 200 μm; bottom panels, 25 μm. ***E***, All SMI-32-positive large neurons in the anterior horn (AHCs, brown color in the cytoplasm) of the cervical cord (C5) were ADAR2 positive (dark gray color in the nuclei) in the control mice (Ctl), whereas some of them were devoid of ADAR2 immunoreactivity in AR2 mice at 2 months of age (2m, arrowheads and inset). Sections were counterstained with hematoxylin. Scale bar: 50 μm; inset, 25 μm.

standard avidin–biotin–immunoperoxidase complex method using the M.O.M. Immunodetection kit (Vector Laboratories) for mouse primary antibodies and Vectastain ABC IgGs (Vector Laboratories) for other primary antibodies. The following primary antibodies were used: mouse anti-nonphosphorylated neurofilament H (SMI-32; dilution at 1:1000; Covance), mouse anti-neuronal nuclei (NeuN) (dilution at 1:500; Millipore Bioscience Research Reagents), sheep anti-rat RED1 (ADAR2) N terminus [dilution at 1:500; a gift from Dr. R. B. Emeson (Sansam et al., 2003)], rabbit anti-glial fibrillary acidic protein (GFAP) (dilution at 1:200; Lab Vision), and rat anti-mouse MAC-2 (dilution at 1:500; Cedarlane). Color was developed with the HRP–DAB System (Vector Laboratories).

Muscles and neuromuscular junctions. Medial gastrocnemius muscles and medial quadriceps muscles were dissected, pinned in mild stretch, and mounted on cork blocks and were quickly frozen in isopentane–liquid nitrogen. Samples were stored at −80°C until use. Five-micrometer-thick transverse frozen sections were stained with hematoxylin and eosin. Twenty-micrometer-thick frozen longitudinal sections were stained with tetramethylrhodamine–bungarotoxin. The same section was incubated with monoclonal antibodies to neurofilament (NF160; dilution at 1:200; Millipore Bioscience Research Reagents) and synaptophysin (dilution at 1:100; Cell Signaling Technologies) and then with Alexa Fluor 488 rabbit anti-mouse IgG (dilution at 1:100; Invitrogen) as the secondary antibody. Stained sections were examined under an LSM-510 confocal microscope system (Carl Zeiss).

Electrophysiology. Mice were anesthetized with isoflurane and placed in a prone position on a thermal pad at 37°C for the examination. Electromyogram (EMG) recordings using a Power Lab 26T and EMG machine (AD Instruments) were obtained using a 29-gauge, Teflon-coated, monopolar needle electrode. The recording electrode was inserted into the gastrocnemius muscles, and spontaneous electrical activity was recorded for 120 s using a Lab Chart analysis system (AD Instruments).

Morphological observation and stereology. Sections of the fifth cervical (C5) and fifth lumbar (L5) spinal cord segments were sequentially immunostained with RED1 and SMI-32 using the HRP–DAB system with and without the addition of $NiCl_2$ for color development. Some sections were immunostained with NeuN. ADAR2-positive and -negative neurons were separately counted among SMI-32-positive neurons with diameters larger than 20 μm in 10 sections for each mouse. The number of NeuN-positive neurons with diameter smaller than 20 μm in the ventral gray matter (ventral to the line running though the ventral edge of the central canal) was counted in 10 C5 sections for each mouse at 12 months of age. None of the NeuN-positive small neurons exhibited SMI-32 or GFAP immunoreactivity. The entire brainstem of each mouse at 12 months of age was cut axially to produce a 10-μm-thick section, and the numbers of all the neurons with nucleoli in the nuclei of cranial motor nerves were counted under a light microscope after cresyl violet staining. The position of each nucleus was stereologically determined using a mouse brain atlas (Paxinos and Franklin, 2001). The positions from the bregma were from −3.80 to −4.24 mm (nucleus of oculomotor nerve), from −4.36 to −4.48 mm (nucleus of trochlear nerve), from −4.84 to −5.34 mm (motor nucleus of trigeminal nerve), from −5.52 to −5.80 mm (nucleus of abducens nerve), from −5.68 to −6.48 mm (nucleus of facial nerve), from −7.08 to −7.92 mm (dorsal nucleus of vagus nerve), and from −7.08 to −8.12 mm (nucleus of hypoglossal nerve). The density of neurons in each nucleus was estimated by dividing the total number of neurons in each nucleus by the volume of the nucleus, which was calculated as the product of the area of the nucleus and the thickness of each section. In addition, transverse, 1-μm-thick, Epon-embedded sections of the anterior horns of the spinal cord, and the ventral roots at the L5 level were prepared and stained with 0.1% toluidine blue. Cell counting was performed by researchers who were blind to the genotype of the mouse.

In situ *hybridization.* Anesthetized mice were perfusion fixed with Tissue Fixative (GenoStaff). Dissected cervical cord tissues were sectioned after they were embedded in paraffin. Antisense and sense *adarb1* cRNA probes (Fig. 1*C*) (supplemental Table S1, available at www.jneurosci.org as supplemental material) were generated from the mouse *adarb1* open reading frame sequence, which was cloned into the pGEMT-Easy vector (Promega). Digoxigenin-labeled cRNA probes were prepared with the DIG RNA Labeling mix (Roche Applied Science). Color was developed with nitro blue tetrazolium/5-bromo-4-chloro-3-indolyl phosphate, and tissue sections were counterstained with Kernechtrot stain solution

(Muto Pure Chemicals). After mounting, 24-bit color images were acquired by scanning of the sections. Digoxigenin signals were isolated by uniformly subtracting the counterstaining color component using Photoshop version 9.0.2 (Adobe Systems) (Ohmae et al., 2006; Takemoto-Kimura et al., 2007).

Statistics. Differences in behavior and survival rates between groups were analyzed using log-rank analysis with SPSS software (version 15; SPSS Inc.), and GraphPad Prism version 4 (GraphPad Software), respectively. The differences in neuronal number between each group and the control samples were examined with a repeated-measures ANOVA. The SPSS version 15 software was used for ANOVA, followed by a Tukey–Kramer statistical test.

Results

Generation of the *ADAR2*$^{flox/flox}$/VAChT–Cre mouse, designated as AR2 mouse

We constructed the mouse *ADAR2*^{flox} allele by flanking exons 7–9 of the *adarb1* gene (mouse *ADAR2* gene) with loxP sites (Fig. 1*A*) (supplemental Table S1, available at www.jneurosci.org as supplemental material). Exons 7–9 encode the majority of the adenosine deaminase motif in the *adarb1* gene (Feng et al., 2006), and Cre-mediated deletion of this region ablates ADAR2 activity. To ablate ADAR2 activity selectively in motor neurons, we crossed *ADAR2*$^{flox/flox}$ mice with VAChT–Cre.Fast mice. In VAChT–Cre.Fast mice, Cre expression is under the control of the vesicular acetylcholine transporter gene promoter, which is active in cholinergic neurons, including spinal motor neurons (Misawa et al., 2003). In these transgenic mice, Cre expression is developmentally regulated, and ~50% of motor neurons express Cre by 5 weeks of age, independent of the heterozygous or homozygous state of the transgene (Misawa et al., 2003). The resulting *ADAR2*$^{flox/flox}$/VAChT–Cre.Fast mice, referred to here as AR2 mice (for breeding, see Materials and Methods), therefore would lack ADAR2 activity in a subset of motor neurons in the spinal cord and other brain motor nuclei after expression of Cre by 5 weeks of age. *In situ* hybridization with a probe encompassing the sequence excised by Cre-mediated recombination (Fig. 1*C*) demonstrated that several large neurons in the anterior horn (AHCs) were devoid of *adarb1* gene signal in the AR2 mice, whereas all the AHCs exhibited the signal in control littermates (Fig. 1*D*). Similarly, a subset of the AHCs were devoid of ADAR2 immunoreactivity in AR2 mice, whereas all AHCs exhibited ADAR2 immunoreactivity in the controls (Fig. 1*E*). There was no difference in the results on male and female AR2 mice.

ADAR2 activity in ADAR2-null motor neurons

Next we examined the effects of recombination of the *ADAR2*^{flox} allele on ADAR2 activity. We dissected all large neurons in the anterior horn (AHCs) (for AHC identification, see supplemental Fig. S1*A*, available at www.jneurosci.org as supplemental material) from frozen sections from 2-month-old AR2 mice ($n = 4$) using a laser microdissector (Fig. 2*A*). We verified that these AHCs, but not small neurons in the anterior horn, are the spinal motor neurons by RT-PCR for choline acetyltransferase on a single-cell lysates (supplemental Fig. S1, available at www.jneurosci.org as supplemental material). Because RT-PCR of GluR2 mRNA on the lysates of three neurons, but not the lysates of one or two motor neurons, reproducibly yielded amplification products, we analyzed the extent of GluR2 Q/R site editing on RNA extracted from the lysates of three pooled AHCs (designated as a specimen) by quantitative analysis of the BbvI-restriction digests of the RT-PCR products, as described previously (Kawahara et al., 2003b, 2004). Among 116 specimens examined, eight showed 0% and 42 showed 100% Q/R site editing, with the remaining 66 specimens distributed between the ranges of 17 and 98% (Fig. 2*A*) (supplemental Table S2, available at www.jneurosci.org as supplemental material). Because AHCs of control littermates (these carried wild-type ADAR2 alleles or no Cre transgene; see Materials and Methods) expressed only edited GluR2 mRNA, the presence of samples exhibiting 0% Q/R site editing suggests that ADAR2-expressing neurons expressed only edited GluR2 mRNA, whereas ADAR2-null neurons expressed only unedited GluR2 mRNA. Then, DNA and total RNA from the specimens were collected in four different groups according to the proportions of unedited GluR2 (Fig. 2*A*). Using PCR, we demonstrated that the samples with 100% editing efficiency (group 0:3) harbored the truncated *ADAR2*^{flox} gene and Cre transcripts, whereas the samples with 100% editing efficiency (group 3:0) carried the full-length *ADAR2*^{flox} gene and did not express Cre (Fig. 2*B*). Those samples with both edited and unedited GluR2 mRNA (groups 1:2 and 2:1) exhibited both full-length and truncated ADAR2 along with the Cre transcript. These qualitative results are consistent with the assumption that recombination of the *ADAR2*^{flox} alleles occurred in a Cre-dependent manner and that this recombination abolished the editing of the GluR2 Q/R site. Among other A-to-I sites examined, we found a significant reduction in editing efficiency only at the GluR6 Q/R site (supplemental Table S3, available at www.jneurosci.org as supplemental material).

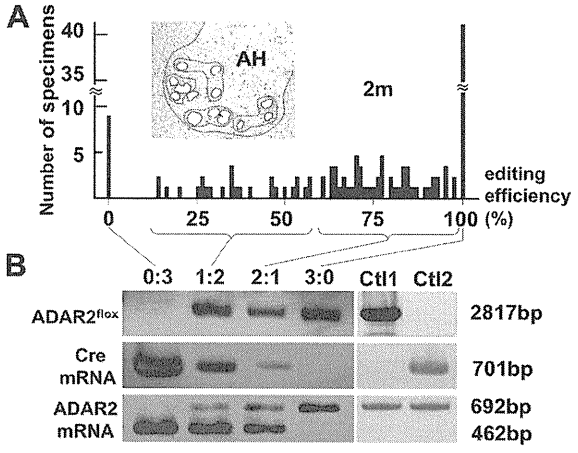

Figure 2. Cre-dependent targeting of ADAR2 and GluR2 Q/R site-editing in motor neurons. ***A***, Frequency histogram of editing efficiency at the GluR2 Q/R site in specimens (lysates containing 3 motor neurons) obtained from AR2 mice at 2 months of age (2m; $n = 4$). Neurons were dissected with a laser microdissector (inset). ***B***, Specimens ($n = 116$) were collected into four groups depending on the predicted number of ADAR2-deficient neurons in each specimen; the groups of specimens containing 3, 2, 1, and 0 unedited GluR2-expressing neurons were designated as groups 0:3, 1:2, 2:1, and 3:0, respectively. The *ADAR2*^{flox} gene and transcripts of the *Cre* gene and the *ADAR2*^{flox} alleles before and after recombination were analyzed for each group by PCR. AHCs expressing unedited GluR2 mRNA (group 0:3) harbored the truncated *ADAR2*^{flox} gene and Cre transcripts, whereas AHCs expressing edited GluR2 mRNA (group 3:0) carried the full-length *ADAR2*^{flox} gene and did not express Cre. Ctl1, *ADAR2*$^{flox/flox}$ mice; Ctl2, VAChT–Cre.Fast mice; AH, anterior horn of the spinal cord.

Behavioral changes

AR2 mice were hypokinetic (supplemental movie, available at www.jneurosci.org as supplemental material) and abnormal in posture (supplemental Fig. S2*A*, available at www.jneurosci.org as supplemental material), but they displayed no overt paralysis or vesico-urinary disturbances and exhibited a normal withdrawal response to noxious stimuli. They showed a lower rotarod performance than their control littermates after 5 weeks of age

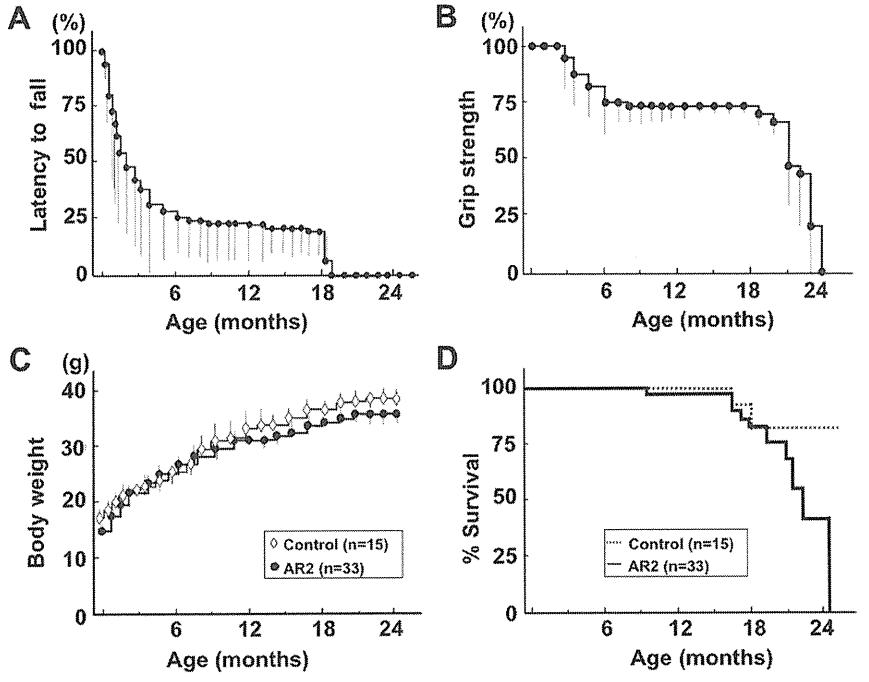

Figure 3. Behavioral changes in AR2 mice. ***A***, Rotarod performance presented as latency to fall (at 10 rpm, 180 s at the maximum) began to decline at 5 weeks of age in AR2 mice and rapidly fell to low levels during the initial 5–6 months, remaining stable until 18 months of age. Control mice exhibited full performance (180 s) until ~12 months of age, followed by slightly lower performance (>164.5 ± 6.4 s) until 24 months. ***B***, Grip strength measured declined with kinetics similar to those of rotarod performance. In ***A*** and ***B***, the scores obtained for the AR2 mice (mean ± SEM; $n = 28$) are indicated as percentage performance of control mice ($n = 15$). ***C***, AR2 mice exhibited slightly lower body weight than controls ($p > 0.05$). ***D***, AR2 mice ($n = 33$) had long lifespans, but the rate of death increased after month 18. The median ± SEM survival was 81.5 ± 16.4 weeks for AR2 mice compared with 105.1 ± 13.5 weeks for control mice ($p = 0.0262$, log-rank analysis).

(Fig. 3*A*), when the Cre expression reached the maximum level (~50% of motor neurons) (Misawa et al., 2003). Their rotarod performance rapidly declined during the initial 5–6 months of life, followed by stable performance until about 18 months of age (Fig. 3*A*). Control mice exhibited full performance (180 s) until ~12 months of age, followed by slightly lower performance (>164.5 ± 6.4 s) until 24 months. Grip strength declined with kinetics similar to those of rotarod performance (Fig. 3*B*). The AR2 mice had slightly lower body weight than the controls (Fig. 3*C*) and were relatively long-lived (81.5 ± 16.4 weeks; mean ± SEM), although not as long as control mice (105.1 ± 13.5 weeks; $p = 0.0262$, log-rank analysis) (Fig. 3*D*).

Pathological alterations in the spinal cords and muscles

Immunohistochemical examination demonstrated that all the AHCs in the spinal cord that were immunoreactive to anti-phosphorylated neurofilament antibodies (SMI-32) showed intense ADAR2 immunoreactivity in their nuclei in control mice, whereas a fraction of these cells was devoid of ADAR2 immunoreactivity in AR2 mice (Fig. 1*E*) (supplemental Fig. S2*B*, available at www.jneurosci.org as supplemental material). There were a number of degenerating AHCs with cytoplasmic vacuoles (Fig. 4*A*) and darkly stained degenerating axons in the ventral roots (Fig. 4*B*). The number of AHCs in AR2 mice markedly decreased between 1 and 2 months of age and then slowly decreased beyond 1 year of age (Fig. 4*C*). The number of ADAR2-positive AHCs in the AR2 mice decreased from 83 to 54% of the number of total AHCs in the age-matched control littermates between 1 and 2 months of age. The rapid reduction in the proportion of ADAR2-positive AHCs during this period is likely attributable to the Cre-dependent recombination of the floxed ADAR2 alleles, because the number of Cre-expressing AHCs in VAChT–Cre-.Fast mice increases developmentally until 5 weeks of age (Misawa et al., 2003). After 2 months of age, the number of ADAR2-positive AHCs did not change over the course of more than 1 year, whereas that of total AHCs decreased from 80 to 54% of the number of AHCs in the age-matched control mice (Fig. 4*C*) (Table 1). Consistent with the Cre-dependent recombination, the proportion of ADAR2-lacking AHCs in AR2 mice is in accordance with that of Cre-expressing AHCs presented in the original study of VAChT–Cre mice (Misawa et al., 2003). Concomitant with AHC degeneration, the number of myelinated axons in the ventral roots was significantly decreased (Table 1).

The kinetics of neuronal loss (Fig. 4*C*) were consistent with the kinetics of progressive motor-selective behavioral deficits (Fig. 3*A*,*B*). The long survival with hypoactivity beyond 6 months of age indicates that the remaining ADAR2-expressing neurons functioned normally during the remainder of life. The high rate of death after 18 months may reflect the failure of the remaining AHCs to compensate for an age-related decline in skeletal muscle power, including a decline in respiratory muscle strength.

We also examined denervation of skeletal muscles. Electromyography performed on AR2 mice at 12 months of age revealed fibrillation potentials and fasciculations, which are common findings in ALS, indicative of muscle fiber denervation and motor unit degeneration and regeneration (Fig. 4*D*). We observed characteristics of denervation, including muscle fiber atrophy, centrally placed nuclei, and pyknotic nuclear clumps in the skeletal muscles of AR2 mice (Fig. 4*E*). Some neuromuscular junctions (NMJs) were not innervated and other NMJs were innervated by ramified axons that innervated more than one NMJ in AR2 mice, indicating reinnervated NMJs (Fig. 4*F*). In contrast, in control mice, all the NMJs were innervated by a single axon. The proportion of denervated NMJs decreased, whereas reinnervated NMJs increased with age in AR2 mice (Fig. 4*F*). In addition, proliferation of activated astrocytes with increased GFAP immunoreactivity and of MAC2-positive activated microglial cells was detected in the anterior horns of AR2 mice (Fig. 4*G*,*H*). These results suggest that degeneration of ADAR2-lacking AHCs induced degeneration of their axon terminals, and then denervated NMJs were reinnervated by collaterally sprouted axons of ADAR2-expressing AHCs after longer survival.

Neurons in the motor nuclei of cranial nerves

The numbers of large neurons in facial and hypoglossal nerve nuclei in AR2 mice were significantly smaller than those in control mice at 12 months of age, whereas the numbers of neurons in nuclei of oculomotor nerves were not decreased (Table 1). Conversely, GluR2 Q/R site editing was significantly decreased both the in oculomotor nerve nuclei (the efficiency of GluR2 Q/R site